Check for updates

Received: 7 February 2022 | Revised: 27 May 2022 | Accepted: 13 July 2022

DOI: 10.1002/fld.5131

RESEARCH ARTICLE

WILEY

Assessment of an adaptive time integration strategy for a high-order discretization of the unsteady RANS equations

Antonio Ghidoni[1] | **Francesco Carlo Massa**[2] | **Gianmaria Noventa**[1] | **Stefano Rebay**[1]

[1]Dipartimento di Ingegneria meccanica e Industriale, Università degli Studi di Brescia, Brescia, Italy

[2]Dipartimento di Ingegneria e Scienze Applicate, Università degli Studi di Bergamo, Dalmine, Italy

Correspondence
Gianmaria Noventa, Dipartimento di Ingegneria meccanica e Industriale, Università degli Studi di Brescia, Via Branze 38, 25123 Brescia, Italy
Email: gianmaria.noventa@unibs.it

Summary

Many industrial applications, for example, aeronautics, aeroacoustics, and turbomachinery, are characterized by complex turbulent flow problems, whose numerical studies are mostly based on statistical models. These models rely on the Navier–Stokes equations averaged in time, namely the Reynolds-averaged Navier–Stokes (RANS) equations. RANS unsteady solutions require accurate and efficient time integration strategies, and the choice of the time-step can have a strong impact on the robustness and efficiency of the simulation. Adaptive time step algorithms can improve considerably the effectiveness of time integration, but in literature little information is available on their application to unsteady RANS equations for high-Reynolds number turbulent flows. This work aims at reducing this gap, presenting a numerical investigation of the performance of different adaptive temporal strategies applied to linearly implicit Rosenbrock-type schemes within a high-order discontinuous Galerkin framework. Several test cases of increasing stiffness and difficulty are considered for both compressible and incompressible turbulent flows.

KEYWORDS

adaptive time integration, discontinuous Galerkin, RANS equations, Rosenbrock-type peer schemes, Rosenbrock-type Runge–Kutta schemes, wind turbine

1 | INTRODUCTION

Discontinuous Galerkin (DG) methods have been emerged as one of the most promising approaches to fluid dynamics computations in many technical areas, including aeronautics, aeroacoustics, and turbomachinery.[1,2] These kind of simulations usually involve the computation of unsteady flows characterized by a wide range of spatial and temporal scales over (very) long time periods. Due to cost considerations, such flow problems are numerically investigated using statistical models. These models solve the Navier–Stokes equations averaged in time, that is the Reynolds-averaged Navier–Stokes (RANS) equations. RANS solutions are commonly stationary, but for some flow problems, for example the flow over a vertical axis wind turbine, unsteady solutions are more appropriate. Accordingly, robust, accurate, and efficient time integration strategies are required.

Explicit and implicit time integration of DG space discretized equations have been already analyzed in the literature. Explicit schemes can achieve very high accuracy, but are limited by Courant-type restrictions. Conversely, although memory demanding due to the storage requirement of the Jacobian matrix, implicit schemes can be designed to be A-stable and

This is an open access article under the terms of the Creative Commons Attribution License, which permits use, distribution and reproduction in any medium, provided the original work is properly cited.
© 2022 The Authors. *International Journal for Numerical Methods in Fluids* published by John Wiley & Sons, Ltd.

L-stable. Several implicit high-order time integration schemes relying on multi-stages and multi-steps have been developed and successfully coupled with DG, for example linearly implicit Rosenbrock-type Runge–Kutta schemes (*A*-stable up to order five),[3,4] Explicit Singly Diagonally Implicit Runge–Kutta (ESDIRK) schemes (*A*-stable up to order five),[5] and linearly implicit Rosenbrock-type two-step peer schemes (*A*- and *L*-stable up to order eight).[6] Rosenbrock-type Runge–Kutta schemes have received increasing attention during the last years as they are linearly implicit, thus requiring to solve only one linear system per each stage and to assemble the Jacobian matrix only once per time step. According to numerical comparisons available in the literature,[3,4] Rosenbrock schemes turned out to be an appealing choice both in terms of accuracy and efficiency.

Generally, the implicit time integration is based on a fixed time step width. This choice can lead to efficiency, robustness, and accuracy issues. On the one hand, if the time-step is too large trying to reduce the computational cost, the simulation could blow-up and/or show accuracy degradation. On the other hand, if the time step is too small, the global number of steps can become extremely large, resulting in an unfeasible simulation. The robustness and computational efficiency of time integration schemes can be improved using adaptive time step strategies. Such algorithms are based on a local error estimator, which exploits the local truncation error of the temporal scheme and of its lower order embedded scheme. An appropriate adaptive strategy aims at guarantee both robustness (large steps and small number of rejected steps) and efficiency (small number of time integration steps for a given accuracy).

In the literature, up to the authors knowledge, little information is available to assess the benefits in terms of robustness, accuracy, and efficiency provided by adaptation strategies for the implicit integration of DG space discretized equations. A deep assessment is available only for the the Navier–Stokes (NS) equations.[7,8] Conversely, no information exists for the unsteady RANS equations, whose solution is more critical than the NS solution, since turbulence models introduce stiffness to the problem. To reduce this gap, the aims of the present work are (*i*) to describe the implementation of several adaptive time step strategies for a high-order discontinuous Galerkin discretization of the unsteady RANS equations, here coupled with the k-$\tilde{\omega}$ turbulence model,[4] (*ii*) to compare the performance of the time integration schemes and adaptive strategies with compressible (system of ODEs) and incompressible (system of DAEs) models, and (*iii*) to show the advantages enabled by time adaptation in terms of robustness and efficiency. Moreover, the outcome of this work could be beneficial also for hybrid RANS–LES simulations, which are spreading in many research areas for the reduced computational cost with respect to the large eddy simulation (LES) approach.

The considered temporal schemes are the linearly implicit one-step Rosenbrock-type Runge–Kutta (third order/three stages ROS3PL,[9] fourth order/six stages RODASP,[10] and fifth order/eight stages ROD5_1[11]) and the linearly implicit Rosenbrock-type two-step peer schemes.[6,12] The controllers adopted for the time adaptation strategy are the standard,[13] the PI 4.2[14] and the H211b and H312b[15] controllers.

Several test cases of increasing stiffness and difficulty are considered: the turbulent flow around a circular cylinder at two different Reynolds numbers $(Re) = \{3900, 140,000\}$, the flow around a tandem cylinders at $(Re) = 166{,}000$, and the turbulent flow through a vertical axis wind turbine (VAWT) at $(Re) = 160{,}000$.[16,17] The first three test cases are used to compare the performance of different combinations between controllers and schemes. The best option in terms of robustness and computational efficiency is used in the last case in order to show the capabilities of the adaptive time integration for challenging turbulent flow problems of industrial interest.

The paper is organized as follows. A quick overview of the governing equations, both for compressible and incompressible flows, and of the discontinuous Galerkin space discretization is given in Sections 2 and 3, respectively. Section 4 describes the time integration schemes, while Section 5 the adaptive time step algorithm with an overview of the most popular error estimators and controllers available in the literature. Section 6 analyzes the performance of the time adaptation in terms of robustness and efficiency for all the proposed test cases. Section 7 summarizes the main conclusions.

2 | GOVERNING EQUATIONS

The complete set of RANS and k-$\tilde{\omega}$ equations[3] for an ideal gas flow can be written as

$$\frac{\partial \rho}{\partial t} + \frac{\partial}{\partial x_j}\left(\rho u_j\right) = 0$$

$$\frac{\partial}{\partial t}\left(\rho e_0\right) + \frac{\partial}{\partial x_j}\left(\rho u_j h_0\right) = \frac{\partial}{\partial x_j}\left[u_i \hat{\tau}_{ji} - q_j\right] - \tau_{ji}\frac{\partial u_i}{\partial x_j} + \beta^* \rho \bar{k} e^{\tilde{\omega}_r}$$

$$
\begin{aligned}
&\frac{\partial}{\partial t}\left(\rho u_i\right)+\frac{\partial}{\partial x_j}\left(\rho u_j u_i\right)=-\frac{\partial p}{\partial x_i}+\frac{\partial \hat{\tau}_{ji}}{\partial x_j}\\
&\frac{\partial}{\partial t}\left(\rho k\right)+\frac{\partial}{\partial x_j}\left(\rho u_j k\right)=\frac{\partial}{\partial x_j}\left[\left(\mu+\sigma^*\overline{\mu}_t\right)\frac{\partial k}{\partial x_j}\right]+\tau_{ji}\frac{\partial u_i}{\partial x_j}-\beta^*\rho\overline{k}e^{\tilde{\omega}_r}\\
&\frac{\partial}{\partial t}\left(\rho\tilde{\omega}\right)+\frac{\partial}{\partial x_j}\left(\rho u_j\tilde{\omega}\right)=\frac{\partial}{\partial x_j}\left[\left(\mu+\sigma\overline{\mu}_t\right)\frac{\partial\tilde{\omega}}{\partial x_j}\right]+\frac{\alpha}{\overline{k}}\tau_{ji}\frac{\partial u_i}{\partial x_j}-\beta\rho e^{\tilde{\omega}_r}+\\
&\qquad+\left(\mu+\sigma\overline{\mu}_t\right)\frac{\partial\tilde{\omega}}{\partial x_k}\frac{\partial\tilde{\omega}}{\partial x_k}+\sigma_d\rho e^{-\tilde{\omega}_r}\max\left(\frac{\partial k}{\partial x_k}\frac{\partial\tilde{\omega}}{\partial x_k},0\right),
\end{aligned}
\tag{1}
$$

where ρ is the fluid density, e_0 and h_0 the stagnation or total energy and enthalpy per unit mass, respectively, while the pressure p, the turbulent and total stress tensor, $\hat{\tau}_{ij}$ and τ_{ij}, the heat flux vector q_j and the eddy viscosity $\overline{\mu}_t$ are given by

$$p=\left(\gamma-1\right)\rho\left(e_0-\frac{u_k u_k}{2}\right), \tag{2}$$

$$\tau_{ji}=2\overline{\mu}_t\left[S_{ij}-\frac{1}{3}\frac{\partial u_k}{\partial x_k}\delta_{ij}\right]-\frac{2}{3}\rho\overline{k}\delta_{ij}, \tag{3}$$

$$\hat{\tau}_{ji}=2\mu\left[S_{ij}-\frac{1}{3}\frac{\partial u_k}{\partial x_k}\delta_{ij}\right]+\tau_{ij}, \tag{4}$$

$$q_j=-\left(\frac{\mu}{Pr}+\frac{\overline{\mu}_t}{Pr_t}\right)\frac{\partial h}{\partial x_j}, \tag{5}$$

$$\overline{\mu}_t=\alpha^*\rho\overline{k}e^{-\tilde{\omega}_r}, \tag{6}$$

with limited value of the turbulent kinetic energy $\overline{k}=\max\left(0,k\right)$ and "realizability" conditions on $\tilde{\omega}_r$. The realizability conditions guarantee that the turbulence model predicts positive normal turbulent stresses and satisfies the Schwarz inequality for shear turbulent stresses.[3] Here $\gamma=\frac{C_p}{C_v}$ is the constant substance specific heat capacities, Pr and Pr_t are the molecular and turbulent Prandtl numbers and

$$S_{ij}=\frac{1}{2}\left(\frac{\partial u_i}{\partial x_j}+\frac{\partial u_j}{\partial x_i}\right), \tag{7}$$

is the mean strain-rate tensor. $\alpha, \alpha^*, \beta, \beta^*, \sigma$, and σ^* are the closure parameters. Notice that the turbulence model equations here used are not in standard form since the variable $\tilde{\omega}=log\left(\omega\right)$ appears instead of ω[3] and $\overline{k}$ is limited exactly to zero, and not to an arbitrary small value, because after the appropriate substitutions no term in the above equations is divided by $\overline{k}$.

When considering an incompressible flow, RANS equations are simplified as

$$
\begin{aligned}
&\frac{\partial u_j}{\partial x_j}=0\\
&\frac{\partial u_i}{\partial t}+\frac{\partial}{\partial x_j}\left(u_j u_i\right)=-\frac{\partial p^*}{\partial x_i}+\frac{\partial \hat{\tau}^*_{ij}}{\partial x_j}\\
&\frac{\partial k}{\partial t}+\frac{\partial}{\partial x_j}\left(u_j k\right)=\frac{\partial}{\partial x_j}\left[\left(\nu+\sigma^*\overline{\nu}_t\right)\frac{\partial k}{\partial x_j}\right]+\tau^*_{ij}\frac{\partial u_i}{\partial x_j}-\beta^*\overline{k}e^{\tilde{\omega}_r}\\
&\frac{\partial\tilde{\omega}}{\partial t}+\frac{\partial}{\partial x_j}\left(u_j\tilde{\omega}\right)=\frac{\partial}{\partial x_j}\left[\left(\nu+\sigma\overline{\nu}_t\right)\frac{\partial\tilde{\omega}}{\partial x_j}\right]+\frac{\alpha}{\overline{k}}\tau^*_{ij}\frac{\partial u_i}{\partial x_j}-\beta e^{\tilde{\omega}_r}+\left(\nu+\sigma\overline{\nu}_t\right)\frac{\partial\tilde{\omega}}{\partial x_k}\frac{\partial\tilde{\omega}}{\partial x_k},
\end{aligned}
\tag{8}
$$

where the density ρ is a constant and

$$p^*=\frac{p}{\rho}\qquad \hat{\tau}^*_{ji}=\frac{\hat{\tau}_{ji}}{\rho}\qquad \tau^*_{ji}=\frac{\tau_{ji}}{\rho}.$$

In the last case, that is, the wind turbine, the flow is around a geometry that operate under an imposed steady rotation, and the governing equations can be rewritten in a reference frame that rotates with the geometry.[18-20] When equations

are solved in a non-inertial reference frame, the momentum conservation equation is augmented by an additional term depending on the centripetal and Coriolis accelerations. According to whether the relative or absolute velocity is considered, the governing equations in the moving frame can be written in two different ways. If the reference frame rotates with a steady angular velocity $\boldsymbol{\omega} = \left[\omega_x, \omega_y, \omega_z\right]^T$ around a rotation center, $\boldsymbol{x}_c = [x_c, y_c, z_c]^T$ the flow velocity can be transformed from the stationary to the moving frame using the relation $\boldsymbol{u}_r = \boldsymbol{u}_a - \boldsymbol{\omega} \times \boldsymbol{r}_c$, where $\boldsymbol{u}_r$ and $\boldsymbol{u}_a$ are the relative and the absolute velocity, respectively, and $\boldsymbol{r}_c = [x - x_c, y - y_c, z - z_c]^T$ is the position vector, pointing from the rotation center to a generic point $[x, y, z]^T$ of the domain. The complete set of RANS and $k - \tilde{\omega}$ equations can be rewritten in the moving frame as

$$
\begin{aligned}
&\frac{\partial \rho}{\partial t} + \frac{\partial}{\partial x_j}\left(\rho u_{r,j}\right) = 0 \\
&\frac{\partial}{\partial t}\left(\rho e_0\right) + \frac{\partial}{\partial x_j}\left(\rho u_{r,j} h_0\right) = \frac{\partial}{\partial x_j}\left[u_{r,i}\hat{\tau}_{ji} - q_j\right] - \tau_{ji}\frac{\partial u_i}{\partial x_j} + \beta^* \rho \overline{k} e^{\tilde{\omega}_r} \\
&\frac{\partial}{\partial t}\left(\rho u_i\right) + \frac{\partial}{\partial x_j}\left(\rho u_{r,j} u_i\right) = -\frac{\partial p}{\partial x_i} + \rho s_{r,i} + \frac{\partial \hat{\tau}_{ji}}{\partial x_j} \\
&\frac{\partial}{\partial t}\left(\rho k\right) + \frac{\partial}{\partial x_j}\left(\rho u_{r,j} k\right) = \frac{\partial}{\partial x_j}\left[\left(\mu + \sigma^* \overline{\mu}_t\right)\frac{\partial k}{\partial x_j}\right] + \tau_{ji}\frac{\partial u_i}{\partial x_j} - \beta^* \rho \overline{k} e^{\tilde{\omega}_r} \\
&\frac{\partial}{\partial t}\left(\rho \tilde{\omega}\right) + \frac{\partial}{\partial x_j}\left(\rho u_{r,j} \tilde{\omega}\right) = \frac{\partial}{\partial x_j}\left[\left(\mu + \sigma \overline{\mu}_t\right)\frac{\partial \tilde{\omega}}{\partial x_j}\right] + \frac{\alpha}{\overline{k}}\tau_{ji}\frac{\partial u_i}{\partial x_j} - \beta \rho e^{\tilde{\omega}_r} + \left(\mu + \sigma \overline{\mu}_t\right)\frac{\partial \tilde{\omega}}{\partial x_k}\frac{\partial \tilde{\omega}}{\partial x_k},
\end{aligned}
\tag{9}
$$

where the source term components $s_{r,i}$ are the sum of the Coriolis and centripetal accelerations, and are defined as

$$
\boldsymbol{s}_r = \begin{pmatrix} \omega_y \hat{u}_z - \omega_z \hat{u}_y \\ \omega_z \hat{u}_x - \omega_x \hat{u}_z \\ \omega_x \hat{u}_y - \omega_y \hat{u}_x \end{pmatrix}, \tag{10}
$$

where $\hat{\boldsymbol{u}} = \boldsymbol{u} + f_r\left(\boldsymbol{u}_r + \boldsymbol{\omega} \times \boldsymbol{r}_c\right)$. The parameter f_r can be set to 0 or 1, depending on whether the unknown variables are considered in the absolute and relative frame, respectively. The total energy and enthalpy per unit mass, e_0 and h_0 respectively, and the pressure p are rewritten as

$$
e_0 = e + \frac{u_k u_k}{2} - f_r \frac{\left(\epsilon_{ijk}\omega_i r_{c,j}\right)\left(\epsilon_{ijk}\omega_i r_{c,j}\right)}{2}, \tag{11}
$$

$$
h_0 = h + \frac{u_k u_k}{2} - f_r \frac{\left(\epsilon_{ijk}\omega_i r_{c,j}\right)\left(\epsilon_{ijk}\omega_i r_{c,j}\right)}{2} - \left(1 - f_r\right) p\left(\epsilon_{ijk}\omega_i r_{c,j}\right), \tag{12}
$$

$$
p = \left(\gamma - 1\right)\rho\left(e_0 - \frac{u_k u_k}{2} + f_r \frac{\left(\epsilon_{ijk}\omega_i r_{c,j}\right)\left(\epsilon_{ijk}\omega_i r_{c,j}\right)}{2}\right), \tag{13}
$$

where e and h are the internal energy and enthalpy, respectively, and ϵ_{ijk} the Levi–Civita tensor.

3 | DG DISCRETIZATION OF THE GOVERNING EQUATIONS

The system of RANS equations for compressible or incompressible flows coupled with the k-$\tilde{\omega}$ turbulence model can be written in compact form as

$$
\mathbf{P}\left(\mathbf{w}\right)\frac{\partial \mathbf{w}}{\partial t} + \nabla \cdot \mathbf{F}_c(\mathbf{w}) + \nabla \cdot \mathbf{F}_v(\mathbf{w}, \nabla \mathbf{w}) + \mathbf{s}(\mathbf{w}, \nabla \mathbf{w}) = \mathbf{0}, \tag{14}
$$

where $\mathbf{w} \in \mathbb{R}^m$ denotes the unknown solution vector of the m variables, the tensors $\mathbf{F}_c, \mathbf{F}_v \in \mathbb{R}^m \otimes \mathbb{R}^d$ denote the inviscid and viscous flux functions, respectively, $\mathbf{s} \in \mathbb{R}^m$ the source terms and d the number of dimensions. In this work the

primitive variables are considered for both compressible $\mathbf{w}_p = \left[p, T, u_i, k, \tilde{\omega}\right]^T$ and incompressible $\mathbf{w}_p = \left[p, u_i, k, \tilde{\omega}\right]^T$ flows. Moreover, in the compressible case, to ensure the positivity of all the thermodynamic variables at the discrete level, the logarithms of pressure $\tilde{p} = \log(p)$ and temperature $\tilde{T} = \log(T)$ are evolved in time.[1,3] In the incompressible case, the matrix $P(\mathbf{w}) \in \mathbb{R}^m \times \mathbb{R}^m$ reduces to a matrix with $P_{i,j} = \delta_{i,j}$, for $i, j = \{2, \cdots, m\}$, being $\delta_{i,j}$ the Kronecker delta and $P_{1,k} = 0$, $P_{k,1} = 0$, for $k = \{1, \cdots, m\}$.

To discretize the governing equations in space, the system (3) is firstly multiplied by an arbitrary smooth test function $\mathbf{v} = \{v_1, \dots, v_m\}$ and then integrated by parts, thus obtaining its weak form. The solution $\mathbf{w}$ and the test function $\mathbf{v}$ are then replaced with a finite element approximation $\mathbf{w}_h$ and a discrete test function $\mathbf{v}_h$ both belonging to $\mathbf{V}_h \overset{\text{def}}{=} [\mathbb{P}_d^k(\mathcal{T}_h)]^m$, where

$$\mathbb{P}_d^k(\mathcal{T}_h) \overset{\text{def}}{=} \left\{ v_h \in L^2(\Omega) \,|\, v_{h|K} \in \mathbb{P}_d^k(K),\ \forall K \in \mathcal{T}_h \right\}, \tag{15}$$

is the discrete polynomial space in physical coordinates. $\mathbb{P}_d^k(K)$ denotes the restriction of the polynomial functions of d variables and total degree $\leq k$ to the element K belonging to the triangulation $\mathcal{T}_h = \{K\}$, consisting of a set of non-overlapping arbitrarily shaped and possibly curved elements, built on an approximation Ω_h of the domain Ω. We also define as $\mathcal{F}_h$ the set of the mesh faces $\mathcal{F}_h \overset{\text{def}}{=} \mathcal{F}_h^i \cup \mathcal{F}_h^b$, where $\mathcal{F}_h^b$ collects the faces located on the boundary of Ω_h and for any $F \in \mathcal{F}_h^i$ there exist two elements $K^+, K^- \in \mathcal{T}_h$ such that $F \in \partial K^+ \cap \partial K^-$. Moreover, for all $F \in \mathcal{F}_h^b$, $\mathbf{n}_F$ is the unit outward normal to Ω_h, whereas, for all $F \in \mathcal{F}_h^i$, $\mathbf{n}_F^-$, and $\mathbf{n}_F^+$ are the unit outward normals pointing to K^+ and K^-, respectively. To deal with discontinuous functions over the internal faces $F \in \mathcal{F}_h^i$ we introduce the jump $[\![\cdot]\!]$ and average $\{\cdot\}$ trace operators, that is

$$[\![v_h]\!] \overset{\text{def}}{=} v_{h|K^+}\mathbf{n}_F^+ + v_{h|K^-}\mathbf{n}_F^-, \qquad \{v_h\} \overset{\text{def}}{=} \frac{v_{h|K^+} + v_{h|K^-}}{2}. \tag{16}$$

When applied to vector functions these operators act componentwise.

Following the approach presented Bassi et al.,[21] for each equation of the system, and without loss of generality, we choose the set of test and shape functions in any element K coincident with the set $\{\phi\}$ of N_{dof}^K orthogonal and hierarchical basis functions in that element. Such basis is built by means of the modified Gram–Schmidt (MGS) algorithm starting from a set of monomials defined over each elementary space $\mathbb{P}_d^k(K)$ in a reference frame relocated in the element barycenter and aligned with the principal axes of inertia of K. Each component $w_{h,j}$, $j = 1, \dots, m$, of the numerical solution $\mathbf{w}_h \in \mathbf{V}_h$ can be expressed, in terms of the elements of the global vector $\mathbf{W}$ of unknown degrees of freedom, as $w_{h,j} = \phi_l W_{j,l}$, $l = 1, \dots, N_{dof}^K$, $\forall K \in \mathcal{T}_h$.

Accounting for these aspects, the DG discretization of the equations consists in seeking, for $j = 1, \dots, m$, the elements of $\mathbf{W}$ such that

$$\begin{aligned}
&\sum_{K\in\mathcal{T}_h} \int_K \phi_i \phi_l \frac{dW_{k,l}}{dt} d\mathbf{x} - \sum_{K\in\mathcal{T}_h} \int_K \frac{\partial \phi_i}{\partial x_n} F_{j,n}\left(\mathbf{w}_h, \nabla_h \mathbf{w}_h + \mathbf{r}\left([\![\mathbf{w}_h]\!]\right)\right) d\mathbf{x} \\
&\quad + \sum_{F\in\mathcal{F}_h} \int_F [\![\phi_i]\!]_n \widehat{F}_{j,n}\left(\mathbf{w}_h^{\pm}, (\nabla_h \mathbf{w}_h + \eta_F \mathbf{r}_F\left([\![\mathbf{w}_h]\!]\right))^{\pm}\right) d\sigma \\
&\quad + \sum_{K\in\mathcal{T}_h} \int_K \phi_i s_j\left(\mathbf{w}_h, \nabla_h \mathbf{w}_h + \mathbf{r}\left([\![\mathbf{w}_h]\!]\right)\right) d\mathbf{x} = 0,
\end{aligned} \tag{17}$$

for $i = 1, \dots, N_{dof}^K$ and where repeated indices imply summation over the ranges $k = 1, \dots, m$, $l = 1, \dots, N_{dof}^K$, and $n = 1, \dots, d$.

In Equation (17), $\mathbf{F}$ denotes the sum of the convective and viscous flux functions, and $\widehat{\mathbf{F}}$ the sum of their numerical counterparts. The DG space discretization of the viscous fluxes is based on the BR2[3] scheme, while the inviscid flux is based on the Godunov flux, computed with an exact Riemann solver. In the incompressible case, an exact Riemann problem associated with a local compressibility perturbation of the Euler equations is adopted.[3] As the perturbation is only included at the level of the flux evaluation, no time derivative for the pressure variable is added to the discrete continuity equation, and resulting in a time-consistent algorithm.

4 | IMPLICIT TIME INTEGRATION

Numerical integration of the DG spatial discretization of RANS equations, Equation (17), by means of suitable Gauss quadrature rules leads to a non-linear ODEs, for compressible flows, or DAEs, for incompressible flows, and can be written as

$$\mathbf{M}_P(\mathbf{W})\frac{d\mathbf{W}}{dt} + \mathbf{R}(\mathbf{W}) = \mathbf{0}, \tag{18}$$

where $\mathbf{R}(\mathbf{W})$ is the vector of residuals and $\mathbf{M}_P(\mathbf{W})$ is the global block diagonal matrix arising from the DG discretization of the governing equations. Thanks to the use of ortho-normal basis functions defined in the physical space and a set of conservative variables the matrix $\mathbf{M}_P$ reduces to the identity matrix for compressible flows and to a modified identity matrix with zeros in the diagonal positions corresponding to the pressure degrees of freedom for incompressible flows. However, for a set of working variables that differs from the conservative one, the transformation matrix $\mathbf{P}$ couples the degrees of freedom of variables within each block of $\mathbf{M}_P$, making the global mass matrix dependent from the solution and no longer diagonal at the element level.

Implicit and accurate time integration of Equation (18) can be efficiently performed by means of linearly implicit time integration schemes. The high-order schemes used in this work are the one-step linearly implicit Rosenbrock-type Runge–Kutta schemes[13] and the linearly implicit two-step peer schemes.[22] In particular, one-step methods[3] show that higher-order schemes are much more efficient than lower-order ones also for the levels of the time integration error typically required by RANS. Table 1 summarizes the properties of the schemes.

Rosenbrock-type and peer schemes entail the solution of linear systems and require the Jacobian evaluation only once per time-step, or less (see Section 4.2). Such features, coupled with higher accuracy, are remarkably favorable for an efficient integration in time. Rosenbrock-type and peer schemes can be designed to be A-stable and L-stable, that is any restriction of the time-step is avoided. However, when they are applied to non-linear systems of DAEs and ODEs, a restriction of the time-step occurs, as they solve a linearized version of the original system at each time-step. For too much large time-step the system linearization can be not enough accurate, resulting in a loss of stability during the time integration, and the blow-up of the simulation. The limit of this instability zone will be called here near-stability zone. Notice that the appearance of this near-stability zone can be seen as a drawback of the class of linearly implicit schemes with respect to the non-linear class that is unconditionally stable.

The linear problems can be efficiently solved in parallel by means of the matrix-explicit or the matrix-free generalized minimal residual (GMRES) method included in the PETSc library. Preconditioning by using the block Jacobin method with one block per process, each solved with ILU(0), or the Additive Schwarz Method (ASM) is usually employed to make GMRES convergence acceptable for complex problems.

4.1 | Linearly implicit Rosenbrock-type Runge–Kutta schemes

The time integration of system (18) by means of one-step linearly implicit Rosenbrock-type schemes, omitting the dependence on $\mathbf{W}$, can be written as

TABLE 1 Properties of the time integration schemes used in this work

	Step	Order	Stage	Order embedded	Stability	Self-starting
ROS3PL	1	3	4	2	A- and L-stable	yes
RODASP	1	4	6	3	A- and L-stable	yes
ROD5_1	1	5	8	4	A- and L-stable	yes
peer3	2	3	3	2	A- and L-stable	no
peer4	2	4	4	3	A- and L-stable	no
peer5	2	5	5	4	A- and L-stable	no

$$\mathbf{W}^{n+1} = \mathbf{W}^n + \sum_{i=1}^{s} b_i \mathbf{K}^i, \tag{19}$$

with $\mathbf{W}^0 = \mathbf{W}\left(t^0\right)$ as initial solution. The vector $\mathbf{K}_i = -\Delta t^n \left(\mathbf{M}_P^{-1}\mathbf{R}\right)^i = -\Delta t^n \tilde{\mathbf{R}}\left(\mathbf{W}^i\right)$ is computed at each stage $i = 1, ..., s$ by solving the linear system

$$\mathbf{K}^i = -\Delta t^n \tilde{\mathbf{R}}\left(\mathbf{W}^n + \sum_{j=1}^{i-1} \alpha_{ij}\mathbf{K}^j\right) - \left(\Delta t \mathbf{M}_P^{-1}\mathbf{J}_P\right)^n \sum_{j=1}^{i} \gamma_{ij}\mathbf{K}^j, \tag{20}$$

where the Jacobian matrix is computed only once per step on the solution $\mathbf{W}^n$. The embedded solution is defined, with $\hat{b}_i$ instead b_i, as

$$\hat{\mathbf{W}}^{n+1} = \mathbf{W}^n + \sum_{i=1}^{s} \hat{b}_i \mathbf{K}^i. \tag{21}$$

This formulation entails the cumbersome matrix-vector product $\mathbf{J}_P^n \sum_{j=1}^{i-1} \gamma_{ij}\mathbf{K}^j$. In practice this can be avoided by means of the following transformation

$$\sum_{j=1}^{i} \gamma_{ij}\mathbf{K}^j = \mathbf{Y}^i \qquad i = 1, ..., s, \tag{22}$$

and thus

$$\mathbf{K}^i = \frac{1}{\gamma_{ii}}\mathbf{Y}^i - \sum_{j=1}^{i-1} c_{ij}\mathbf{Y}^j \qquad i = 1, ..., s, \tag{23}$$

for which Equations (19) and (20) can be reduced to the equivalent formulation

$$\begin{aligned} &\mathbf{W}^{n+1} = \mathbf{W}^n + \sum_{j=1}^{s} m_j \mathbf{Y}^j, \\ &\left(\frac{\mathbf{M}_P}{\gamma_{ii}\Delta t} + \mathbf{J}_P\right)^n \mathbf{Y}_i = -\mathbf{M}_P^n \left[\tilde{\mathbf{R}}\left(\mathbf{W}^n + \sum_{j=1}^{i-1} a_{ij}\mathbf{Y}^j\right) + \sum_{j=1}^{i-1} \frac{c_{ij}}{\Delta t^n}\mathbf{Y}^j\right], \end{aligned} \tag{24}$$

and

$$\hat{\mathbf{W}}^{n+1} = \mathbf{W}^n + \sum_{i=1}^{s} \hat{m}_i \mathbf{Y}^i, \tag{25}$$

α_{ij}, γ_{ij}, b_i, $\hat{b}_i$, a_{ij}, c_{ij}, m_i, and $\hat{m}_i$ are real coefficients of the two formulations uniquely define the Rosenbrock scheme and are related by the equations

$$\begin{aligned} &\left(c_{ij}\right) = \text{diag}\left(\gamma_{11}^{-1}, ..., \gamma_{ss}^{-1}\right) - \Gamma^{-1}, \\ &\left(a_{ij}\right) = \left(\alpha_{ij}\right)\Gamma^{-1}, \\ &(m_1, ..., m_s) = (b_1, ..., b_s)\Gamma^{-1}, \\ &(\hat{m}_1, ..., \hat{m}_s) = \left(\hat{b}_1, ..., \hat{b}_s\right)\Gamma^{-1}, \end{aligned}$$

where $\Gamma \equiv \left(\gamma_{ij}\right)$ and $\gamma_{ii} = \gamma \neq 0$. "Traditional" Rosenbrock-type schemes, for example, ROS3PL, RODASP, and ROD5_1, may suffer from order reduction for very stiff problems. To overcome this limitation, recently, new types of linearly implicit Rosenbrock-type schemes have been proposed in literature.[7]

The incompressible laminar traveling waves and the compressible inviscid isentropic vortex cases are here used to prove the correctness of the implementation of the schemes and to assess the behavior with ODEs and DAEs, respectively. In both the cases the analytical solution allows to calculate the error and to prove the exact order of convergence of the schemes. In the former the traveling wave solution of the NS equations on the doubly-periodic unit square $[0.25, 1.25] \times [0.5, 1.5]$ is considered, with the analytical solution defined as

$$u_1(x, y, t) = 1 + 2\cos(2\pi(x - t))\sin(2\pi(y - t))\, e^{-8\pi^2 \nu t}, \tag{26}$$

$$u_2(x, y, t) = 1 - 2\sin(2\pi(x - t))\cos(2\pi(y - t))\, e^{-8\pi^2 \nu t}, \tag{27}$$

$$p(x, y, t) = -(\cos(4\pi(x - t)) + \cos(4\pi(y - t)))\, e^{-16\pi^2 \nu t}, \tag{28}$$

with $\nu = 1e^{-2}$. In the latter the inviscid isentropic vortex transported by a uniform flow is considered, with the Euler equations. The vortex is defined by velocity and temperature perturbations of a uniform flow, with pressure, temperature, and density equal to 1 and with velocity components equal to $\sqrt{\gamma}$, where $\gamma = 1.4$ is the ratio of specific heats. The perturbations are given by

$$\delta u_1 = -\alpha \frac{\alpha}{2 * \pi}(y - y_0)\, e^{\phi(1-r^2)}, \tag{29}$$

$$\delta u_2 = \alpha \frac{\alpha}{2 * \pi}(x - x_0)\, e^{\phi(1-r^2)}, \tag{30}$$

$$\delta T = -\frac{\alpha^2(\gamma - 1)}{16\phi\gamma\pi^2} e^{2\phi(1-r^2)}, \tag{31}$$

where $\phi = 1/2$, $\alpha = 5$, and r is the distance of a point (x, y) from the vortex center (x_0, y_0) placed at $(5, 5)$ in a periodic domain $[0, 10] \times [0, 10]$ at time $t_0 = 0$. To verify the order of convergence of all the schemes, the solutions are computed using a very accurate DG-$\mathbb{P}^6$ space discretization on a uniform 50×50 quadrilateral elements with linear edges mesh, resulting in 70,000 degrees of freedom per equation (DOFs) for both cases.

The convergence order of the schemes are first verified, considering time-steps $\Delta t \in \{T/400, T/40\}$ where the linear system tolerances is set to $tol_{System} = 10^{-16}$. Figures 1 and 2 show the L^2 norm of the pressure error ($\|err_p\|_2$) as a function of the time-step, while Tables 2 and 3 summarize the results, providing the L^2 norm of the pressure and velocity components ($\|err_{u_x}\|_2$, $\|err_{u_y}\|_2$) errors, and the convergence order for the traveling waves and the isentropic vortex. All schemes verify the convergence order, 3 for ROS3PL, 4 for RODASP, and 5 for ROD5_1, for both cases. Time convergence errors below 1E-11 are affected by the spatial accuracy, and this is clearly visible in the degradation of the order of convergence of the ROD5_1 for the smallest time-step.

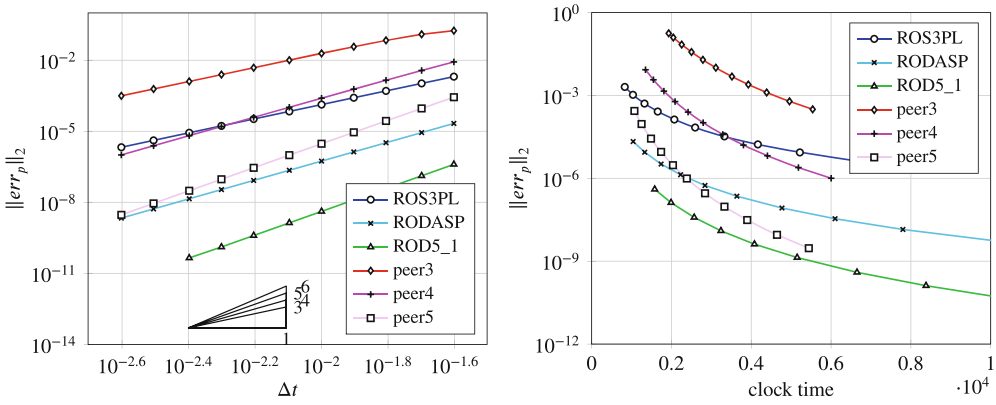

FIGURE 1 Traveling waves. L^2 norm of the pressure error ($\|err_p\|_2$) as a function of the time-step Δt (left) and the clock time [*wu*] (right), $tol_{System} = 10^{-16}$, and discontinuous Galerkin (DG)-$\mathbb{P}^6$ solution approximation

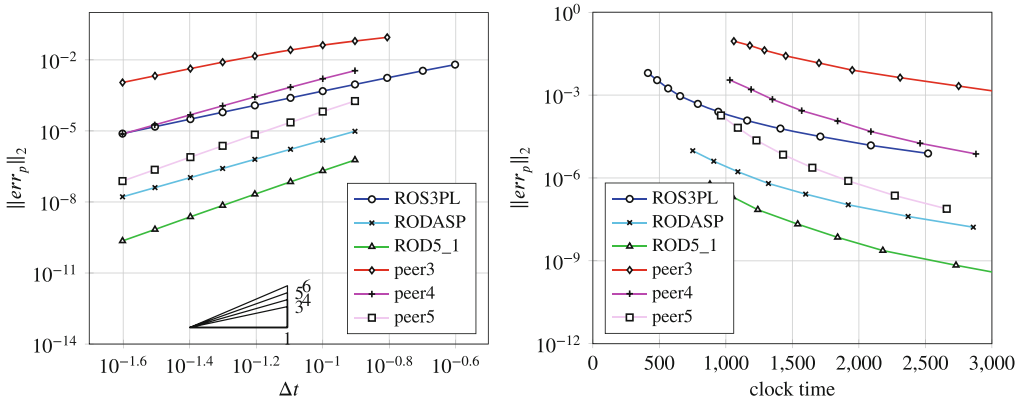

FIGURE 2 Isentropic vortex. L^2 norm of the pressure error ($\|err_p\|_2$) as a function of the time-step Δt (left) and the clock time [wu] (right), $tol_{System} = 10^{-16}$, and discontinuous Galerkin (DG)-$\mathbb{P}^6$ solution approximation

TABLE 2 Traveling waves. L^2 norm of the pressure ($\|err_p\|_2$) and velocity components ($\|err_{u_x}\|_2$, $\|err_{u_y}\|_2$) errors, and convergence order for ROS3PL, RODASP, ROD5_1 schemes, $tol_{System} = 10^{-16}$, and DG-$\mathbb{P}^6$ solution approximation

	Δt	$\|err_p\|_2$	Order	$\|err_{u_1}\|_2$	Order	$\|err_{u_2}\|_2$	Order
ROS3PL	T/40	2.04E-03	2.94	3.13E-03	2.94	3.13E-03	2.94
	T/80	2.62E-04	2.98	4.03E-04	2.98	4.03E-04	2.98
	T/160	3.30E-05	2.99	5.08E-05	2.99	5.08E-05	2.99
	T/320	4.14E-06	3.00	6.37E-06	3.00	6.37E-06	3.00
	T/400	2.12E-06	—	3.26E-06	—	3.26E-06	—
RODASP	T/40	2.15E-05	3.99	3.35E-05	4.00	3.35E-05	4.00
	T/80	1.35E-06	4.00	2.10E-06	4.00	2.10E-06	4.00
	T/160	8.43E-08	4.00	1.31E-07	4.00	1.31E-07	4.00
	T/320	5.27E-09	4.00	8.20E-09	4.00	8.20E-09	4.00
	T/400	2.16E-09	—	3.36E-09	—	3.36E-09	—
ROD5_1	T/40	4.02E-07	4.99	6.23E-07	4.98	6.23E-07	4.98
	T/80	1.26E-08	4.99	1.96E-08	4.99	1.96E-08	4.99
	T/160	3.96E-10	5.00	6.16E-10	4.99	6.16E-10	4.99
	T/320	4.79E-11	2.90	1.94E-11	4.49	1.94E-11	4.49
	T/400	2.50E-11	—	7.12E-12	—	7.12E-12	—

Abbreviation: DG, discontinuous Galerkin.

4.2 | Linearly implicit two-step peer schemes

Peer schemes[23] are a class of Rosenbrock-type schemes proposed to overcome the order reduction of the "traditional" Rosenbrock-type schemes with high-stiffness. They take a linear combination of stages values to approximate the exact solution at intermediate points. All stages values have the same order of accuracy and the same stability properties, which is the reason for calling the method "peer". Conversely, in one-step schemes intermediate stages solutions have lower order than the final solution. Peer schemes up to order eight are available and are characterized by good stability properties, strong damping properties at infinity without further restrictions, and robustness with respect to step-size changes. Since all stages solutions have the same accuracy and stability properties, a continuous high-order output is also available with no extra-cost. As all multi-step schemes, peer schemes are not self-starting and, thus, they need a starting procedure in order to obtain required initial solutions.

TABLE 3 Isentropic vortex. L^2 norm of the pressure ($\|err_p\|_2$), temperature ($\|err_p\|_2$), and velocity components ($\|err_{u_1}\|_2$, $\|err_{u_2}\|_2$) errors, and convergence order for ROS3PL, RODASP, ROD5_1 schemes, $tol_{System} = 10^{-16}$, and DG-$\mathbb{P}^6$ solution approximation

	Δt	$\|err_p\|_2$	Order	$\|err_T\|_2$	Order	$\|err_{u_1}\|_2$	Order	$\|err_{u_2}\|_2$	Order
ROS3PL	T/40	6.31E-03	2.68	2.82E-03	2.60	9.30E-03	2.78	8.83E-03	2.59
	T/80	9.20E-04	2.92	4.28E-04	2.89	1.31E-03	2.91	1.34E-03	2.89
	T/160	1.20E-04	2.98	5.63E-05	2.97	1.71E-04	2.97	1.76E-04	2.97
	T/320	1.51E-05	3.00	7.12E-06	2.99	2.16E-05	2.99	2.22E-05	2.99
	T/400	7.72E-06	—	3.65E-06	—	1.11E-05	—	1.14E-05	—
RODASP	T/40	—	—	—	—	—	—	—	—
	T/80	9.67E-06	3.91	3.75E-06	3.92	1.82E-05	3.95	1.74E-05	3.90
	T/160	6.31E-07	3.97	2.43E-07	3.97	1.16E-06	3.99	1.14E-06	3.97
	T/320	4.04E-08	4.02	1.55E-08	4.02	7.37E-08	4.02	7.30E-08	4.02
	T/400	1.65E-08	—	6.34E-09	—	3.00E-08	—	2.98E-08	—
ROD5_1	T/40	—	—	—	—	—	—	—	—
	T/80	5.93E-07	4.72	2.57E-07	4.64	7.60E-07	4.72	9.61E-07	4.83
	T/160	2.13E-08	4.98	9.57E-09	4.97	2.74E-08	4.96	3.25E-08	4.98
	T/320	6.90E-10	4.98	3.15E-10	4.97	9.17E-10	4.93	1.06E-09	4.93
	T/400	2.27E-10	—	1.04E-10	—	3.05E-10	—	3.52E-10	—

Abbreviation: DG, discontinuous Galerkin.

The solution approximations $\mathbf{W}^{i,n} \sim \mathbf{W}\left(t^n + c_i \Delta t^n\right)$, with $i = 1, ..., s$, of the system (18) can be calculated by means of s linear systems

$$\left(\frac{\mathbf{M}_P^{s,n-1}}{\gamma \Delta t^n} + \mathbf{J}_P^{s,n-1}\right)\left(\mathbf{W}_{i,n} - \mathbf{W}_0 * i\right) = -\mathbf{M}_P^{s,n-1}\left(\tilde{\mathbf{R}}_0^{i,n} + \frac{\mathbf{Y}^i - \mathbf{W}_0^i}{\gamma \Delta t^n}\right), \tag{32}$$

with

$$\mathbf{Y}_i = \sum_{j=1}^{i-1} \frac{a_{ij}}{\gamma}\left(\mathbf{W}^{j,n} - \mathbf{Y}^j\right) + \sum_{j=1}^{s} u_{ij}\left(\sigma^n\right)\mathbf{W}^{j,n-1}, \tag{33}$$

$$\mathbf{W}_0^i = \sum_{j=1}^{i-1} \frac{a_{0,ij}}{\gamma}\left(\mathbf{W}^{j,n} - \mathbf{Y}^j\right) + \sum_{j=1}^{s} u_{0,ij}\left(\sigma^n\right)\mathbf{W}^{j,n-1}, \tag{34}$$

where s is the number of stages and the Jacobian matrix of the DG space discretization $\mathbf{J}_P^{s,n-1}$ is computed only once per step with the last stage solution of the previous step $\mathbf{W}^{s,n-1}$. At each step, the embedded solution is given by

$$\hat{\mathbf{W}}^{s,n} = \sum_{i=1}^{s-1} \alpha_i \mathbf{W}^{i,n}. \tag{35}$$

$\mathbf{A} = \{a_{ij}\}$, $\mathbf{U} = \{u_{ij}\}$, $\mathbf{A}_0 = \{a_{0ij}\}$, and $\mathbf{U}_0 = \{u_{0ij}\}$ are $s \times s$ matrices of real coefficients and α_i, c_i, and γ are real parameters. Matrices $\mathbf{U}$ and $\mathbf{U}_0$ depend on the step size ratio $\sigma^n = \Delta t^n / \Delta t^{n-1}$ between current and previous time-step in order to ensure accuracy and stability properties for variable time-step. More in general, matrices $\mathbf{A}$, $\mathbf{U}$, $\mathbf{A}_0$, and $\mathbf{U}_0$ and parameters γ and c_i uniquely define accuracy and stability properties of an s-stages peer scheme.

Consistency and zero stability conditions that ensure an order of accuracy equal to $s - 1$ for all peer stages and for all step size ratios $\sigma > 0$ are provided in Podhaisky et al.[23] and Gerisch et al.[22] These conditions are derived independently from the Jacobian matrix which thus can be computed numerically, for example, by means of finite differences. Matrices

$\mathbf{A}$, $\mathbf{U}$, $\mathbf{A}_0$, and $\mathbf{U}_0$ are only functions of parameters c_i and γ, where coefficients c_i are chosen to be stretched Chebychev nodes in the interval $[-1, 1]$, that is,

$$c_i = -\frac{\cos\left(\left(i - \frac{1}{2}\right)\frac{\pi}{s}\right)}{\cos\left(\frac{\pi}{2s}\right)} \qquad i = 1, ..., s. \tag{36}$$

Following this choice, it is clear that $c_s = 1$, and thus

$$\mathbf{W}^{n+1} = \mathbf{W}^{s,n} \qquad \hat{\mathbf{W}}^{n+1} = \hat{\mathbf{W}}^{s,n}. \tag{37}$$

The last parameter γ specifies the θ angle of $A(\theta)$- and $L(\theta)$-stability. Moreover, as demonstrated by Podhaisky et al.[23] only for constant time-steps, specific values of γ can guarantee an additional order of accuracy, which becomes equal to the number of stages s. Finally, coefficients α_i with $i = 1, ..., s-1$ are only function of nodes c_i and are computed such that the order of the embedded solution is equal to $\hat{q} = s - 2$.[22] Peer methods used in this work have three, four, and five stages, where the parameter γ for each scheme is reported in Table 4. For these values, peer methods show an order of accuracy equal to s.

The validation for peer schemes is shown in Figures 1 and 2, while Tables 5 and 6 summarize the results, providing the L^2 norm of the pressure and velocity components errors and the convergence order. All schemes verify the convergence

TABLE 4 List of γ values and corresponding θ angles of $A(\theta)$-stability and $L(\theta)$-stability for each peer scheme used in this work

	s	γ	θ
peer3	3	$2.165162598341552E+00$	90°
peer4	4	$1.038881828680110E+00$	90°
peer5	5	$5.614731292097847E-01$	90°

TABLE 5 Traveling waves. L^2 norm of the pressure ($\|err_p\|_2$) and velocity components ($\|err_{u_x}\|_2$, $\|err_{u_y}\|_2$) errors, convergence order for peer schemes with exact initialization, $tol_{System} = 10^{-16}$, and DG-$\mathbb{P}^6$ solution approximation

	Δt	$\|err_p\|_2$	Order	$\|err_{u_x}\|_2$	Order	$\|err_{u_y}\|_2$	Order
peer3	T/40	1.78E-01	1.57	2.76E-01	1.57	2.76E-01	1.57
	T/80	3.74E-02	2.92	5.82E-02	2.92	5.82E-02	2.92
	T/160	4.84E-03	2.98	7.54E-03	2.98	7.54E-03	2.98
	T/200	2.49E-03	2.98	3.88E-03	2.98	3.88E-03	2.98
	T/400	3.15E-04	—	4.90E-04	—	4.90E-04	—
peer4	T/40	8.53E-03	3.74	1.33E-02	3.73	1.33E-02	3.73
	T/80	6.01E-04	3.93	9.36E-04	3.93	9.36E-04	3.93
	T/160	3.88E-05	3.98	6.04E-05	3.98	6.04E-05	3.98
	T/320	2.45E-06	3.99	3.82E-06	3.99	3.82E-06	3.99
	T/400	1.01E-06	—	1.57E-06	—	1.57E-06	—
peer5	T/40	2.75E-04	4.89	4.28E-04	4.89	4.28E-04	4.89
	T/80	9.07E-06	4.97	1.41E-05	4.97	1.41E-05	4.97
	T/160	2.87E-07	4.99	4.47E-07	4.99	4.47E-07	4.99
	T/320	9.02E-09	5.00	1.40E-08	5.01	1.40E-08	5.01
	T/400	2.96E-09	—	4.60E-09	—	4.60E-09	—

Abbreviation: DG, discontinuous Galerkin.

TABLE 6 Isentropic vortex. L^2 norm of the pressure ($\|err_p\|_2$) and velocity components ($\|err_{u_x}\|_2$, $\|err_{u_y}\|_2$) errors, convergence order for peer schemes with exact initialization, $tol_{System} = 10^{-16}$, and DG-$\mathbb{P}^6$ solution approximation

	Δt	$\|err_p\|_2$	Order	$\|err_T\|_2$	Order	$\|err_{u_x}\|_2$	Order	$\|err_{u_y}\|_2$	Order
peer3	T/40	—	—	—	—	—	—	—	—
	T/80	6.25E-02	1.80	2.26E-02	1.52	1.56E-01	2.26	1.10E-01	2.04
	T/160	1.45E-02	2.65	6.16E-03	2.50	2.61E-02	3.03	2.36E-02	2.86
	T/320	2.12E-03	2.91	9.75E-04	2.88	3.23E-03	3.02	3.13E-03	2.96
	T/400	1.11E-03	—	5.13E-04	—	1.65E-03	—	1.62E-03	—
peer4	T/40	—	—	—	—	—	—	—	—
	T/80	3.50E-03	3.52	1.47E-03	3.56	6.66E-03	3.55	5.91E-03	3.37
	T/160	2.73E-04	3.88	1.11E-04	3.93	5.11E-04	3.91	4.91E-04	3.86
	T/320	1.80E-05	3.98	7.12E-06	4.00	3.31E-05	3.99	3.27E-05	3.97
	T/400	7.41E-06	—	2.92E-06	—	1.36E-05	—	1.35E-05	—
peer5	T/40	—	—	—	—	—	—	—	—
	T/80	1.83E-04	4.59	8.78E-05	4.57	3.03E-04	4.61	3.22E-04	4.58
	T/160	6.98E-06	4.88	3.38E-06	4.88	1.14E-05	4.90	1.23E-05	4.89
	T/320	2.30E-07	4.95	1.12E-07	4.97	3.73E-07	4.96	4.04E-07	4.95
	T/400	7.64E-08	—	3.68E-08	—	1.23E-07	—	1.34E-07	—

Abbreviation: DG, discontinuous Galerkin.

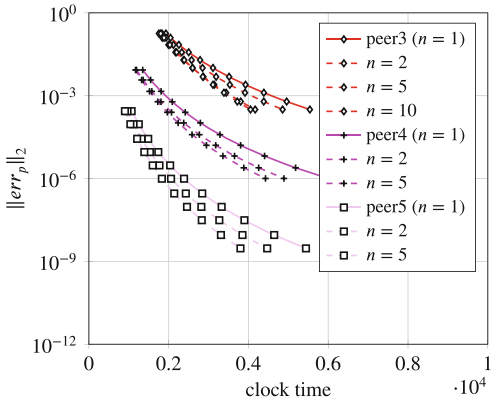

FIGURE 3 Traveling waves. L^2 norm of the pressure error ($\|err_p\|_2$) as a function of the clock time [wu] for peer schemes with the Jacobian matrix calculated every n time-steps (with $n = 1, 2, 5$, and 10), $tol_{System} = 10^{-16}$, and discontinuous Galerkin (DG)-$\mathbb{P}^6$ solution approximation

order, 3 for peer3, 4 for peer4, and 5 for peer5, for both cases. The performance of the peer schemes deteriorate in the compressible case, that is, with ODEs.

Peer schemes can use an inexact Jacobian matrix, while traditional one-step Rosenbrock schemes need to compute the exact Jacobian matrix at each time-step. This feature allows to freeze the Jacobian matrix during the simulation, reducing the computational cost. Figure 3 shows the L^2 norm of the pressure error as a function of the computational time, for the peer schemes, where the Jacobian freezing leads to a reduction of the computational time for all the schemes. However, the number of time-steps before the recalculation of the Jacobian matrix is limited, because above a threshold (10 for peer3 and 5 for peer4 and peer5) the computational saving is lost due to the inefficient solution of the linear system. The computational saving increases for lower error levels, and its maximum value for peer5 is around 24% at $\Delta t = T/200$.

Finally, peer schemes are multi-step and, as all multi-step methods, are not self-starting. Starting solutions $\mathbf{W}^{i,0}$ with $i = 1, ..., s$ at times

$$t^{i,0} = t^{st} + c_i \Delta t^{st} \qquad i = 1, ..., s, \tag{38}$$

where

$$\Delta t^{st} = t^1 - t^{st}, \tag{39}$$

must be initialized in order to compute the solution corresponding to the first time-step, that is, $\mathbf{W}^{s,1}$ for the Equation (32). Gerisch et al.[22] suggest to compute starting solutions using one time step of a one-step method with continuous output and to control their accuracy by means of standard adaptive time step algorithm or by choosing Δt^{st} sufficiently small. However, this strategy, even if straightforward and fast, has three main drawbacks: (*i*) the one-step method must provide a continuous output, (*ii*) the continuous output, in general, has a different accuracy with respect to the one-step method and this must be taken into account for the choice of the starting step-size Δt^{st}, and (*iii*) for continuous output with low order of accuracy the starting step-size can be excessively small, leading to a large first step-size ratio $\sigma^1 = \Delta t^1 / \Delta t^{st}$ that reduces the peer order from s to $s - 1$. In order to overcome these drawbacks Massa et al.[6] introduced a new starting procedure for peer methods based on the local and global asymptotic behaviors of time integration errors.

Defining

$$c^- = \min_{i \in [1,s]} (c_i) \qquad t^- = t^{st} + c^- \Delta t^{st}, \tag{40}$$

as the minimum value of nodes c_i, and the smallest time point t^i of the starting procedure, respectively, and imposing $t^- = t^0$ with t^0 the initial time, it follows from Equation (38) that

$$t^{i,0} = t^0 + (c_i - c^-) \Delta t^{st} \qquad i = 1, ..., s, \tag{41}$$

and from Equation (39)

$$t^1 = t^0 + (1 - c^-) \Delta t^{st}. \tag{42}$$

The starting procedure time-step Δt^{st} is here imposed equal to the user-defined initial time-step Δt^1 of peer methods, that is, $\Delta t^{st} = \Delta t^1$, in order to ensure $\sigma^1 = 1$. Moreover, the starting procedure time integration period can be derived from Equation (41) as

$$T^{st} = \left(c^+ - c^-\right) \Delta t^{st}, \tag{43}$$

with $c^+ = \max_{i \in [1,s]} (c_i)$.

Starting solutions at corresponding times $t^{i,0}$ can be obtained by means of a one-step time integration scheme, for example, a Rosenbrock-type scheme with global order q'_g and local order q'_l, because for small time integration periods T' the asymptotic behavior of the global error can be written in a more general form

$$\|err_{T'}\| \propto \left(T'\right)^x \left(\Delta t'\right)^y,$$

where $\Delta t'$ is the arithmetic mean value of the step size during the time integration of the one-step scheme and the exponents x and y can be defined from global and local error definitions noting that

$$\|err_{T'}\| \propto \left(\overline{\Delta t'}\right)^y \propto \left(\overline{\Delta t'}\right)^{q'_g} \qquad T' = const,$$
$$\|err_{T'}\| \propto \left(\overline{\Delta t'}\right)^{x+y} \propto \left(\overline{\Delta t'}\right)^{q'_l} \qquad T' = \Delta t',$$

that means

$$x = q'_l - q'_g, \qquad y = q'_g. \tag{44}$$

Imposing then a starting solution accuracy proportional to the accuracy of the peer scheme used for the simulation, the following relation can be found

$$(T\prime)^{q'_l - q'_g} (\Delta t\prime)^{q'_g} \propto (\Delta t)^{q_g}, \tag{45}$$

where Δt is the arithmetic mean time-step used by the peer scheme of order q_g. Knowing that $T' = T^{st}, \Delta t \sim \Delta t^1$, the mean step-size of the one-step method is derived from Equation (45), as

$$\Delta t' = \psi \left(\Delta t^1\right)^{\frac{q_g + q'_g - q'_l}{q'_g}}, \tag{46}$$

where the constant value must be defined by the user (for simplicity $\psi = 1$). After sorting the starting time points such $t_j^0 < t_{j+1}^0$, $j = 1, ..., s-1$, with in general $t_j^0 \neq t_i^0$ for $j = i$, the number of steps required to integrate in time from t_j^0 to t_{j+1}^0 by means of the one-step scheme can be found as

$$N'_j = \text{int}\left(\frac{t_{j+1}^0 - t_j^0}{\Delta t'}\right) + 1. \tag{47}$$

As consequence, the corresponding fixed time-step is

$$\Delta t'_j = \frac{t_{j+1}^0 - t_j^0}{N'_j}. \tag{48}$$

Notice that $\Delta t'_j \leq \Delta t'$. Finally, imposing the initial condition

$$\mathbf{W}^{j=1,0} = \mathbf{W}\left(t^0\right), \tag{49}$$

the solution $\mathbf{W}^{j+1,0}$ with $j = 1, ..., s-1$ can be computed starting from $\mathbf{W}^{j,0}$ after N'_j steps of dimension $\Delta t'_j$ performed with the one-step temporal scheme. This procedure can be applied to a generic one-step scheme independently on its accuracy, and without requiring any dense output, meanwhile ensuring the accuracy of the peer method. However, the suggestion is to avoid the use of this strategy for $q'_g << q_g$, since from Equation (46) the step-size $\Delta t'$ could become too small, leading to an excessively expensive starting procedure. Furthermore, since it is not ensured in general that a one-step method provides the same order of accuracy for all system variables, the exponent in Equation (46) is set for safety purposes as the maximum exponent computed for each variable w_k.

$$\frac{q_g + q'_g - q'_l}{q'_g} = \max_{k \in [1,m]} \left(\frac{q_g + q'_g - q'_l}{q'_g}\right)_{w_k}. \tag{50}$$

For example in the incompressible waves case the initial solution can be given also using an one-step schemes (ROS3PL, RODASP, and ROD5_1 schemes of Section 4.1). Table 7 summarizes the results, with different one-step schemes used for the initialization, providing the L^2 norm of the pressure and velocity components errors, and the computational time. Notice that peer schemes, regardless of the one-step scheme adopted in the numerical starting procedure, and preserve the global accuracy. Nevertheless, with a lower order one-step scheme the starting procedure becomes more expensive, thus reducing the overall efficiency of a peer scheme.

5 | ADAPTIVE TIME-STEP STRATEGY

Automatic step-size control is an important feature for the efficiency and robustness of time integration schemes. Fixed time steps typically result in a large number of small steps, leading to large computational costs. Adaptive time-step can

TABLE 7 Traveling waves. L^2 norm of the pressure and velocity components errors, convergence order, and the clock time [*wu*] for peer schemes with numerical starting procedure, $tol_{System} = 10^{-15}$, and DG-$\mathbb{P}^6$ solution approximation

	Δt	$\|err_p\|_2$	Order	$\|err_{u_x}\|_2$	Order	$\|err_{u_y}\|_2$	Order	CPU time [*wu*]
peer3 (ROS3PL)	T/40	1.78E-01	1.57	2.76E-01	1.57	2.76E-01	1.57	2.66E+03
	T/80	3.74E-02	2.92	5.82E-02	2.92	5.82E-02	2.92	3.02E+03
	T/160	4.84E-03	2.98	7.54E-03	2.98	7.54E-03	2.98	3.88E+03
	T/320	6.13E-04	2.99	9.54E-04	2.99	9.54E-04	2.99	5.58E+03
	T/400	3.15E-04	—	4.90E-04	—	4.90E-04	—	6.55E+03
peer4 (ROS3PL)	T/40	8.52E-03	3.74	1.33E-02	3.73	1.33E-02	3.73	1.78E+03
	T/80	6.01E-04	3.93	9.35E-04	3.93	9.35E-04	3.93	2.22E+03
	T/160	3.88E-05	3.98	6.04E-05	3.98	6.04E-05	3.98	3.28E+03
	T/320	2.45E-06	3.99	3.81E-06	3.99	3.81E-06	3.99	6.16E+03
	T/400	1.01E-06	—	1.57E-06	—	1.57E-06	—	7.15E+03
peer5 (RODASP)	T/40	2.75E-04	4.89	4.29E-04	4.89	4.29E-04	4.89	1.60E+03
	T/80	9.07E-06	4.97	1.41E-05	4.97	1.41E-05	4.97	2.14E+03
	T/160	2.87E-07	4.99	4.47E-07	4.99	4.47E-07	4.99	3.62E+03
	T/320	9.02E-09	5.00	1.40E-08	5.00	1.40E-08	5.00	6.03E+03
	T/400	2.96E-09	—	4.60E-09	—	4.60E-09	—	7.63E+03
peer5 (ROS3PL)	T/40	2.75E-04	4.89	4.29E-04	4.89	4.29E-04	4.89	1.54E+03
	T/80	9.08E-06	4.97	1.41E-05	4.97	1.41E-05	4.97	2.25E+03
	T/160	2.87E-07	4.99	4.48E-07	4.99	4.48E-07	4.99	3.89E+03
	T/320	9.03E-09	4.99	1.41E-08	5.00	1.41E-08	5.00	7.50E+03
	T/400	2.96E-09	—	4.61E-09	—	4.61E-09	—	7.78E+03

Abbreviation: DG, discontinuous Galerkin.

instead substantially improve the simulation effectiveness by (*i*) reducing the number of time steps, and, therefore, minimizing the computational effort, required to achieve a user-defined accuracy level and by (*ii*) improving the robustness of the computation as a result of lower local truncation error values during the time integration process. In general, to increase the robustness and efficiency of a simulation, the selected temporal scheme should work at the maximum allowable time-step, associated to the near-stability zone, and to the physical time scales of the problem that should be solved. An adaptive time-step strategy, based on a local error estimator overcomes these limitations, allowing to go beyond the near-stability zone of the scheme.

An adaptive time integration strategy can be based, following the idea put forward by Söderlind and Wang,[24] on three different "error types":

- Global error at time t^{n+1}, that is, the numerical error of the time integration, defined as the difference between the exact $\mathbf{w}\left(t^{n+1}\right)$ and the numerical $\mathbf{w}^{n+1}$ solution

$$err^{n+1} = \|\mathbf{w}\left(t^{n+1}\right) - \mathbf{w}^{n+1}\|, \tag{51}$$

  where $\|\cdot\|$ denotes some user defined norm;
- Local truncation error (LTE), that is, the numerical error introduced by the temporal scheme at the single time-step level

$$LTE^{n+1} = \|\mathbf{w}\left(t^{n+1}\right) - \mathbf{w}_{\star}^{n+1}\|, \tag{52}$$

  where $\mathbf{w}_{\star}^{n+1}$ is the solution approximation computed applying one step of the prescribed temporal scheme starting from the exact solution $\mathbf{w}\left(t^{n}\right)$ or $(\mathbf{w}\left(t^{n-1} + c_{i=1,\dots,s}\Delta t^{n-1}\right)$ for peer methods). Since the exact solution $\mathbf{w}(t)$ is in general

not available for complex problems except for the initial condition $\mathbf{w}^0 = \mathbf{w}\left(t^0\right)$, the LTE can be approximated as

$$LTE^1 = \mathbf{w}(t^1) - \mathbf{w}_\star^1 \approx \mathbf{w}_r^1 - \mathbf{w}^1, \tag{53}$$

where $\mathbf{w}^1$ is the numerical solution, while $\mathbf{w}_r^1$ is a reference numerical solution more accurate than $\mathbf{w}^1$;

- Local estimator, defined by means of the embedded solution $\hat{\mathbf{w}}(t)$ as

$$r^{n+1} = \|\mathbf{w}^{n+1} - \hat{\mathbf{w}}^{n+1}\|, \tag{54}$$

which can be cheaply computed at each time-step, conversely to the LTE.

Each "error type" can be represented by means of an asymptotic model: $err^{n+1} = \psi_g^{n+1}(\Delta t)^{q_g}$, $LTE^{n+1} = \psi_l^{n+1}(\Delta t^n)^{q_l}$, and $r^{n+1} = \psi_r^{n+1}(\Delta t^n)^{q_r}$. ψ_g, ψ_l, and ψ_r are the global, local, and estimator constants, and q_g, q_l, and q_r are the global, local, and estimator orders of convergence. Δt is the arithmetic mean of the time-steps during the time integration, and is defined as:

$$\Delta t = \frac{1}{N}\sum_{k=1}^{N}\Delta t^{k-1}, \tag{55}$$

where N is the number of performed steps at time t^{n+1}. The adaptive temporal approach consists in choosing the step-size Δt^n to guarantee a constant LTE during the simulation. LTE cannot be computed when the analytic solution is unavailable, and is, therefore, approximated as a function of the local estimator $LTE^{n+1} \approx f\left(r^{n+1}\right)$.

This hypothesis allows to build the adaptive algorithm on r^{n+1}, that is, if the algorithm is able to maintain r^{n+1} constant as much as possible during the simulation, the LTE will be constant as well. In practice, the standard adaptive time-step algorithm[15,24] requires at each time step that

$$r^{n+1} < \mu TOL, \tag{56}$$

where TOL is a user-defined adaptive tolerance and $\mu = \{3/2, 2\}$ is a user-defined safety factor ($\mu = 2$ in this work). If this condition is verified, the solution $\mathbf{w}^{n+1}$ is accepted, and the next step-size Δt^{n+1} is computed as:

$$\Delta t^{n+1} = \left(\frac{r^{n+2}}{\psi_r^{n+2}}\right)^{\frac{1}{q_r}} = \left(\frac{TOL}{\psi_r^{n+2}}\right)^{\frac{1}{q_r}}, \tag{57}$$

where $r^{n+2} = TOL$. Otherwise, $\mathbf{w}^{n+1}$ is rejected, and the step is repeated with a smaller Δt^n given by

$$\Delta t^n = \left(\frac{TOL}{\psi_r^{n+1}}\right)^{\frac{1}{q_r}}, \tag{58}$$

where the constant ψ_r^{n+1} is obtained from the local estimator $\overline{r}^{n+1}$ and the rejected time-step $\overline{\Delta t}^n$, as

$$\psi_r^{n+1} = \frac{\overline{r}^{n+1}}{\left(\overline{\Delta t}^n\right)^{q_r}}. \tag{59}$$

The only unknown quantity in the above relations is the estimator constant ψ_r^{n+2} appearing in Equation (57), which must be effectively predicted by the interpolation of the ψ values available at previous time steps. In practice, introducing the logarithmic variable $\tilde{\psi}_r = \ln(\psi)$, the interpolation can be written as

$$\tilde{\psi}_r^{n+2} \approx \sum_{j=1}^{z}\alpha_j\tilde{\psi}_T^{n+2-j} + \sum_{j=1}^{z}\beta_j\tilde{\psi}_r^{n+2-j}, \tag{60}$$

thus obtaining

$$\psi_r^{n+2} = \prod_{j=1}^{z} \left(\psi_T^{n+2-j}\right)^{\alpha_j} \prod_{j=1}^{z} \left(\psi_r^{n+2-j}\right)^{\beta_j}, \tag{61}$$

where z is the number of past values used, α_j and β_j are real coefficients and

$$\psi_T^{n+2-j} = \frac{TOL}{\Delta t^{n+1-j}} \qquad j = 1, \cdots, z. \tag{62}$$

Notice that, due to the logarithmic variables, the predicted estimator constant is always positive regardless of the α_j and β_j values. By combining Equations (57) and (61) and by considering different sets of α_j and β_j coefficients, the following so called proportional integral (PI) controllers for the computation of Δt^{n+1} can be obtained

$$\Delta t^{n+1} = \Delta t^n \left(\frac{TOL}{r^{n+1}}\right)^{\frac{1}{q_r}}, \tag{63}$$

$$\Delta t^{n+1} = \Delta t^n \left(\frac{TOL}{r^{n+1}}\right)^{\frac{3}{5q_r}} \left(\frac{TOL}{r^n}\right)^{\frac{-1}{5q_r}}, \tag{64}$$

$$\Delta t^{n+1} = \Delta t^n \left(\frac{\Delta t^n}{\Delta t^{n-1}}\right)^{-\frac{1}{4}} \left(\frac{TOL}{r^{n+1}}\right)^{\frac{1}{4q_r}} \left(\frac{TOL}{r^n}\right)^{\frac{1}{4q_r}}, \tag{65}$$

$$\Delta t^{n+1} = \Delta t^n \left(\frac{\Delta t^n}{\Delta t^{n-1}}\right)^{-\frac{3}{8}} \left(\frac{\Delta t^{n-1}}{\Delta t^{n-2}}\right)^{-\frac{1}{8}} \left(\frac{TOL}{r^{n+1}}\right)^{\frac{1}{8q_r}} \left(\frac{TOL}{r^n}\right)^{\frac{1}{4q_r}} \left(\frac{TOL}{r^{n-1}}\right)^{\frac{1}{8q_r}}. \tag{66}$$

The above controllers are named standard (see Equation (63)),[13] PI 4.2 (see Equation (64)),[14] H211b (see Equation (65)), and H312b (see Equation (66)),[15] and are the most popular controllers in literature and are used in this work to evaluate and compare their performance. The coefficients α_j and β_j are reported in Table 8. Note that the consistency condition $\sum_{j=1}^{z} \alpha_j + \beta_j = 1$ is always verified.

While for the LES approach the error estimator r^{n+1} can be written as a function of only one unknown j, that is, $r^{n+1} = r_j^{n+1} = \|w_j^{n+1} - \hat{w}_j^{n+1}\|_2$ because unknown fields are quite smooth, for the RANS approach it is mandatory to compute the error estimator r^{n+1} as a function of all solution variables w_j to include also the turbulent variables k and $\tilde{\omega}$, which show often an irregular distribution and are the main reason of the simulation instability:

$$r^{n+1} = \sqrt{\sum_{j=1}^{m} \left(r_j^{n+1}\right)^2}. \tag{67}$$

Notice that the average of r_j over the domain is not enough to guarantee robustness, and the L^2 norm is mandatory. Moreover, only the use of the turbulent variables for the computation of r could provide too small time-steps.

The robustness and the efficiency of the controllers can be substantially improved by limiting the maximum possible increase/reduction of Δt, with:

- a smooth limiter function

$$\Delta t^{n+1} = \Delta t^n \left[1 + \kappa \arctan\left(\frac{\Delta t^{n+1} - \Delta t^n}{\kappa \Delta t^n}\right)\right], \tag{68}$$

TABLE 8 Real coefficients α_j and β_j for each adaptive time-step controller used in this work

	z	α_1	α_2	α_3	β_1	β_2	β_3
Standard	1	0	—	—	1	—	—
PI 4.2	2	2/5	1/5	—	3/5	−1/5	—
H211b	2	2/4	0	—	1/4	1/4	—
H312b	3	4/8	0	0	1/8	2/8	1/8

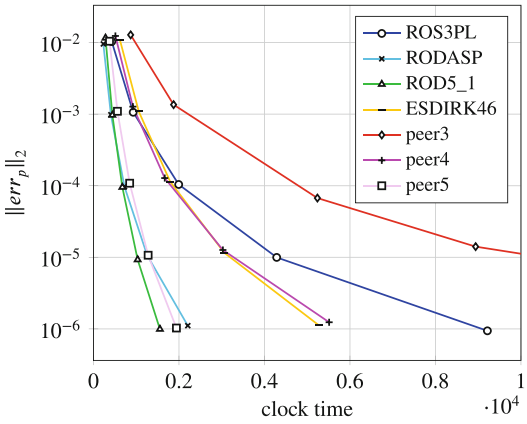

FIGURE 4 Traveling waves. L^2 norm of the pressure error ($\|err_p\|_2$) as a function of the clock time [wu], $tol_{System} = 10^{-16}$, and discontinuous Galerkin (DG)-$\mathbb{P}^6$ solution approximation

where the value of the parameter κ is usually set in the range $[0.7, 2]$.[14] In this work the effect of the smooth limiter function has been analyzed for the H221b controller, and it called H211b-smooth;

- a correction factor η

$$\Delta t^{n+1} = \eta \Delta t^{n+1}; \tag{69}$$

- a maximum allowed time-step Δt_{limit}, that is,

$$\Delta t^{n+1} = \min\left(\eta \Delta t^{n+1}, \Delta t_{\text{limit}}\right). \tag{70}$$

The target of the adaptive algorithm is to control the global error of the computation, while the parameter that drives the adaptive procedure is the relative tolerance TOL. It is however possible to devise a procedure so that the tolerance TOL becomes in fact equal to the required global error. This requires an appropriate calibration, see for example, Söderlind and Wang,[24] that must be performed for any time integration shemes before the actual computation. For example considering the incompressible waves, Figure 4 shows the L^2 norm of the pressure error as a function of the computational time after the tolerance calibration procedure, where each scheme works in the proportional mode.

6 | NUMERICAL RESULTS

The performance of the proposed adaptive algorithm applied to implicit temporal schemes is investigated in terms of robustness and efficiency, that is, accuracy and computational time, both for compressible and incompressible cases of increasing stiffness and difficulty: the turbulent flow around a circular cylinder at two different Reynolds numbers $Re = \{3900, 140, 000\}$ and the turbulent flow around a tandem cylinders at $Re = 166{,}000$. Finally, the proposed approach is applied for the solution of the turbulent flow through a vertical axis wind turbine. In all the cases the turbulent flow is described through the unsteady RANS equations coupled with the k-$\tilde{\omega}$ turbulence model.[4]

In the first three test cases the initial transient phase starts from a DG $\mathbb{P}^1$ steady solution and the polynomial degree is gradually increased up to $\mathbb{P}^5$. During this phase, for each increment of the polynomial degree the ROS3PL time integration scheme is adopted with an integration interval equal to $3T$, as T is the vortex shedding period. After the transient phase, the simulations are advanced in time for a period T using the constant step-size or the adaptive algorithm with different controllers. The constant time step width is prescribed according to the following relation: $\Delta t = 2^{-i}T/5$, where $i = 0, ..., 6$, while for the adaptive strategies the tolerance is set as $TOL = 10^{-i}$ with $i = 3, ..., 8$. Solution errors are defined with respect to a reference solution obtained for each test case with the ROD5_1 scheme and $\Delta t = T/3264$. The meshes are generated with a $2D$ high-order version of a fully automated in-house hybrid mesh generator based on the Advancing-Delaunay strategy.[25] The non-dimensional height of the first element near wall is $y_1^+ < 4$, where thanks to the high-order spatial discretization the y_1^+ is below one from the DG-$\mathbb{P}^3$ discretization. All the computations are performed on a Linux cluster

with 12 AMD 6220 CPUs (8 cores per CPU). The clock time is reported in tables and figures as a normalized value with respect to the *TauBenchmark*[26] value, $t_{TauBench}$, obtained on a full node of the cluster used for the CFD simulation*. The normalized computing time is measured as work units (wu) and is defined as $wu = (\text{clocktime} \times n_{cores})/t_{TauBench}$, where n_{cores} is the numbers of cores.

In the following, peer schemes are not considered for compressible solver cases since the isentropic vortex test case showed a worst performance with respect to Rosenbrock schemes. Furthermore only the compressible solver is used for the more complex cases since proved to be more efficient. This is strictly related to the efficiency of the solution of the linear system. In fact, due to the nature of DAEs, in the incompressible solver the linear system is worse conditioned resulting in a lower convergence speed in comparison with the compressible solver. Where this outcome becomes more and more prominent as the test case complexity increases.

6.1 | Turbulent flow around a circular cylinder at $Re = 3900$

The turbulent flow around a circular cylinder at sub-critical Reynolds number $Re = 3900$, based on the cylinder diameter and the freestream quantities, is here considered. In order to investigate the performance of the controller of the adaptive time-step strategy and the time integration schemes with ODEs and DAEs this test case is considered both with the compressible and incompressible solver. In the former the Mach number is $M = 0.1$ to consider the flow essentially incompressible. In sub-critical flow regime, the boundary layer is laminar until the separation, where the transition takes place in the separated shear layer. The phenomenology of the flow field in the wake of the cylinder is largely driven by the laminar-turbulent transition of the shear layer with the creation of Kelvin–Helmholtz instabilities with the break-up of the shear layer and an asymmetric Von Kármán vortex shedding. RANS can be expected to provide accurate results.[27] The mesh has 4037 hybrid elements, triangles, and quadrilaterals, with quadratic edges and the solution is obtained with a very high-order DG-$\mathbb{P}^5$ discretization, resulting in 84,777 DOFs per equation. Figure 5 shows the instantaneous x-component velocity and turbulent intensity contours.

The literature shows a very wide documentation for this test case, which can be considered as a benchmark for turbulent flows. Reference data covers the most important integral, such as the forces on the wall (pressure coefficient and vorticity) and the wake dynamics behind the cylinder (velocity profiles, first- and second-order statistics profiles). For the integrals on the wall Norberg[28] described pressure measurements on the cylinder for $Re = 3000$ while Son and Hanratty[29] the wall vorticity for $Re = 5000$. For the first-order statistics Ong and Wallace,[30] who managed to accurately measure velocity and vorticity vectors in the near wake outside the recirculation bubble and proposed turbulence profiles and power spectra of the components of the velocity at several locations between $4 \leq x/D \leq 10$. Lourenco and Shih[31] described measurements also in the recirculation region of the flow ($1.06 \leq x/D \leq 10$) where statistical quantities were assessed even though this PIV experiment was not designed for this purpose. Nevertheless, these results were used as reference of several numerical simulations, for example, Mittal and Moin[32] and Wissink and Rodi.[33] Recently, the flow around a circular cylinder at $Re = 3900$ was studied both numerically, with LES, and experimentally, with particle image velocimetry (PIV) and hot-wire anemometry (HWA) methods, by Parnaudeau et al.[31] The PIV data of

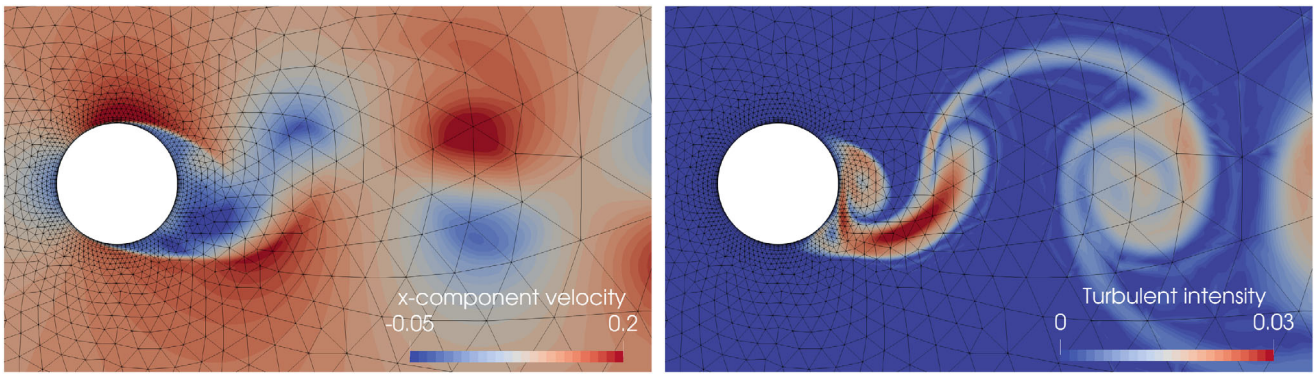

FIGURE 5 Cylinder $Re = 3900$. Instantaneous x-component velocity (left) and turbulent intensity (right) contours in the compressible case, discontinuous Galerkin (DG)-$\mathbb{P}^5$ solution approximation

TABLE 9 Cylinder $Re = 3900$. Comparison of the root-mean-square lift coefficient $c_{L\,rms}$, the time-averaged drag coefficient c_D, the Strouhal number St, the time-averaged separation angles θ_{sep}, the time-averaged base suction coefficient $-c_{p\,b}$, the time-averaged peak of the stream-wise velocity in the wake $-u_{min}/u_{\inf}$, and the time-averaged recirculation zone length L_r/D, between literature and results

	c_D	$c_{L\,rms}$	St	$-c_{p\,b}$	L_r/D	$-u_{min}/u_\infty$	θ_{sep}
Lourenco and Shih exp.[31]	0.99	—	0.22	—	1.19	0.24	86°
Norberg exp.[28]	0.98	0.04-0.15	—	0.9	—	—	—
Ong and Wallace exp.[30]	—	—	0.21	—	—	—	—
Ma et al. DNS[35]	0.84	—	0.22	—	1.59	—	—
Parnaudeau et al. exp.[31]	—	—	0.21	—	1.51	0.34	—
Parnaudeau et al. LES[31]	—	—	0.21	—	1.56	0.28	—
Wissink and Rodi DNS[33]	—	—	0.22	—	1.588	0.33	87°
Breuer LES[36]	1.04	—	0.2	0.94	1.35	0.37	88°
Lysenko LES Smag.[34]	1.18	0.44	0.19	0.8	0.9	0.26	89°
Lysenko LES k-eq.[34]	0.97	0.09	0.209	0.91	1.67	0.27	88°
Rajani et al. RANS 2D[27]	1.65	—	0.24	2.02	—	0.28	102°
Rajani et al. RANS 3D[27]	1.27	—	0.22	1.51	0.31	0.09	98°
RANS DG-$\mathbb{P}^5$ comp.	1.62	1.13	0.23	1.84	—	0.43	87°
RANS DG-$\mathbb{P}^5$ inc.	1.52	1.13	0.23	1.90	—	0.43	86°

Abbreviations: LES, large eddy simulation; RANS, reynolds-averaged Navier–Stokes; DG discontinuous Galerkin.

Parnaudeau et al.[31] differs from Lourenco and Shih,[31] while are at the same time similar with the HWA data of Ong and Wallace.[30]

Several high-fidelity LES, or implicit LES, and DNS were carried out during the last two decades. The first to perform a numerical analysis with a LES for this test case was Beaudan and Moin.[32] In recent years the work by Lysenko et al.[34] is of particular interest, where simulations were carried out to understand the different accuracy of sub-grid scale models for LES, that is, a conventional Smagorinsky and a dynamic k-equation eddy viscosity. Wissink and Rodi performed a DNS at $Re = 3300$ in order to study the influence of the span-wise length of the computational domain, with results perfectly consistent with the experiments of Parnaudeau et al.[31] and Rajani et al.[27] performed three-dimensional unsteady RANS and LES and two-dimensional unsteady RANS in order to compare the accuracy of RANS with respect to higher-fidelity simulations and the accuracy of two-dimensional simulations with respect to three-dimensional simulations.

The time-averaged drag coefficient here obtained for the incompressible solver is $c_D = 1.52$, the root mean square of the lift coefficient is $c'_L = 1.13$, and the Strouhal number is $St = 0.23$, while for the compressible solver $c_D = 1.62$, $c'_L = 1.19$, and $St = 0.225$. Table 9 summarizes the results in comparison with experiment and other numerical results. In particular, the root-mean-square lift coefficient $c_{L\,rms}$, the time-averaged drag coefficient c_D, the Strouhal number St, the time-averaged separation angles θ_{sep}, the time-averaged base suction coefficient $-c_{p\,b}$, the time-averaged peak of the stream-wise velocity in the wake $-u_{min}/u_{\inf}$, and the time-averaged recirculation zone length L_r/D are reported. The separation angle θ_{sep} is computed from the condition of vanishing wall-shear stresses in the time-averaged field around the cylinder, while the base suction coefficient $-c_{p\,b}$ as the time-averaged pressure coefficient distribution on the cylinder at $\theta = 180°$ ($x = 0.5$, $y = 0$), where the stagnation point is at $\theta = 0°$ ($x = -0.5$, $y = 0$). The results are different in comparison to the high-fidelity simulations or the experiment, but in good agreement with other two-dimensional unsteady RANS numerical results. In fact, DNS or LES are able to capture the strong three-dimensional perturbations introduced by the circular cylinder. For example, Rajani et al.[27] showed $c_D = 1.65$ and $St = 0.244$ on two-dimensional mesh with 120×145 elements, while $c_D = 1.27$ and $St = 0.225$ on three dimensional mesh with $120 \times 145 \times 32$, where these results spotlight the discrepancy between two- and three-dimensional simulations. This difference can be ascribed to the inability of the two-dimensional simulations to capture the strong three-dimensional features that characterize this type of flows. However, the objective of this work is not to correctly predict complex turbulent flow phenomena, but to assess in terms of computational efficiency and robustness adaptive time-step strategies for turbulent flows. Figure 6 shows the time-averaged pressure coefficient c_p and non-dimensional wall vorticity $\Omega/2Re^{0.5}$ distribution on the cylinder in

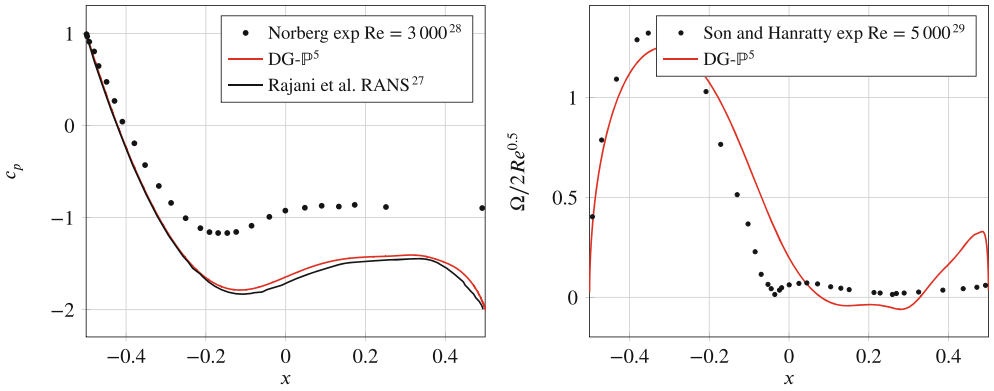

FIGURE 6 Cylinder $Re = 3900$. Time-averaged pressure coefficient c_p (left) and non-dimensional wall vorticity $\Omega/2Re^{0.5}$ (right) distribution on the cylinder, discontinuous Galerkin (DG)-$\mathbb{P}^5$ solution approximation

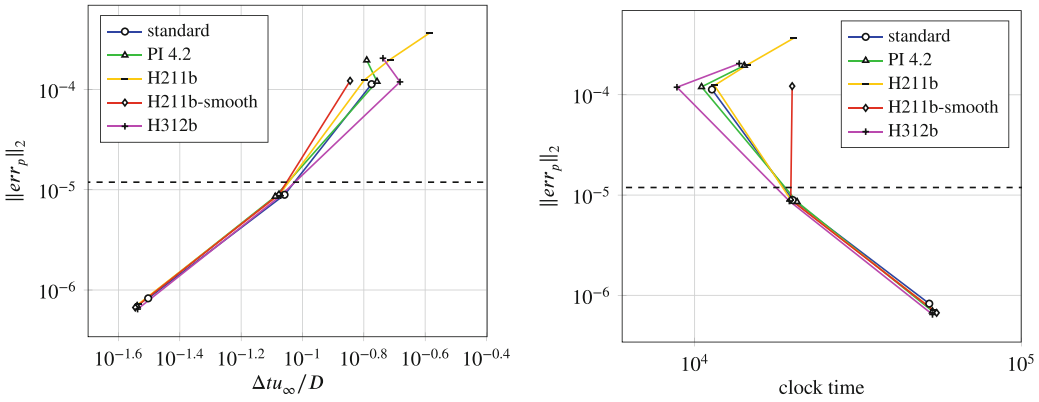

FIGURE 7 Cylinder $Re = 3900$. L^2 norm of the pressure error ($\|err_p\|_2$) as a function of the time-averaged time-step $\Delta t u_\infty / D$ and the clock time [wu] with different controller in the compressible case, ROS3PL scheme with $tol_{system} = 10^{-14}$ and discontinuous Galerkin (DG)-$\mathbb{P}^5$ solution approximation. The horizontal dashed line represents the limit of stability of the scheme with constant time-steps, that is, without the adaptive time-step strategy

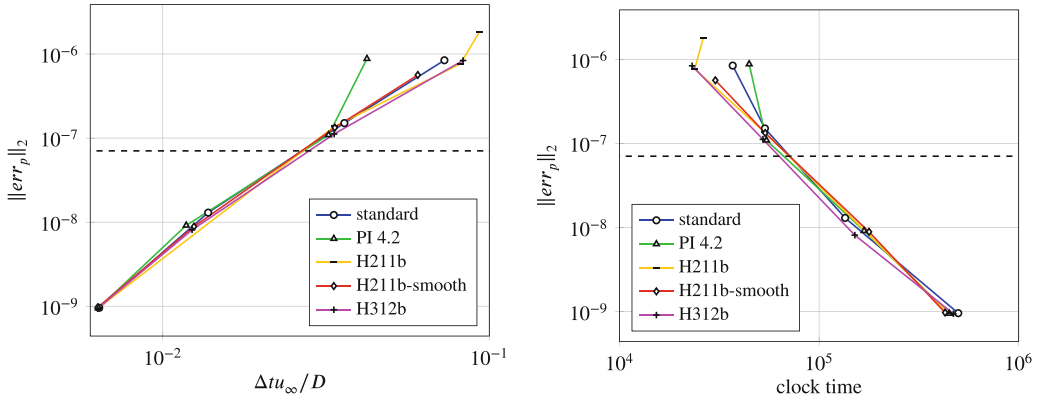

FIGURE 8 Cylinder $Re = 3900$. L^2 norm of the pressure error ($\|err_p\|_2$) as a function of the time-averaged time-step $\Delta t u_\infty / D$ and the clock time [wu] with different controller in the compressible case, RODASP scheme with $tol_{system} = 10^{-14}$ and discontinuous Galerkin (DG)-$\mathbb{P}^5$ solution approximation. The horizontal dashed line represents the limit of stability of the scheme with constant time-steps, that is, without the adaptive time-step strategy

comparison with experiment, by Norberg[28] and Son and Hanratty[29] respectively for c_p and $\Omega/2Re^{0.5}$, and the numerical results of Rajani et al.[27] in the two-dimensional case.

Figures 7–9 show the performance of the different controller in the compressible case with ROS3PL, RODASP, and ROD5_1. The L^2 norm of the pressure error $\|err_p\|_2$ is depicted as a function of the time-averaged time-step $\Delta tu_\infty/D$ and the clock time. Figures 10 and 12 show the evolution of the adaptive time-step $\Delta tu_\infty/D$ with different levels of error. In particular, the former shows the performance of ROS3PL and different controllers, while the latter shows the performance of ROD5_1 with H211b-smooth controller and different κ values. Decreasing the time-step no differences are appreciable

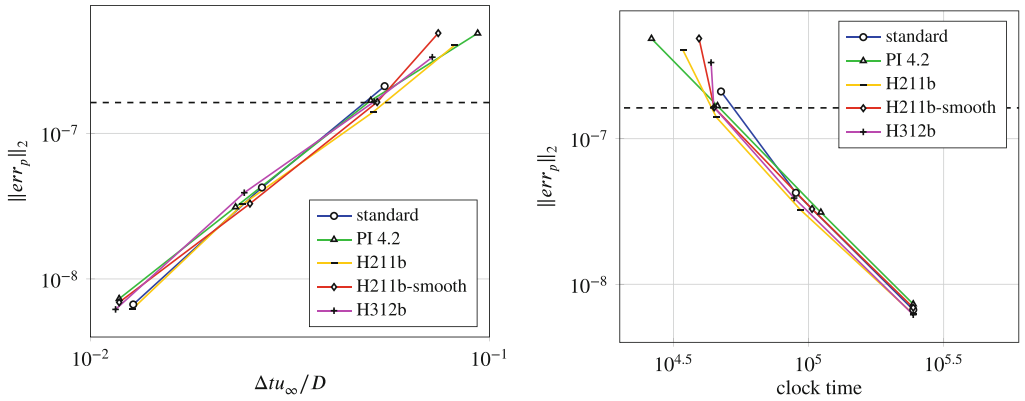

FIGURE 9 Cylinder $Re = 3900$. L^2 norm of the pressure error ($\|err_p\|_2$) as a function of the time-averaged time-step $\Delta tu_\infty/D$ and the clock time [wu] with different controller in the compressible case, ROD5_1 scheme with $tol_{system} = 10^{-14}$ and discontinuous Galerkin (DG)-$\mathbb{P}^5$ solution approximation. The horizontal dashed line represents the limit of stability of the scheme with constant time-steps, that is, without the adaptive time-step strategy

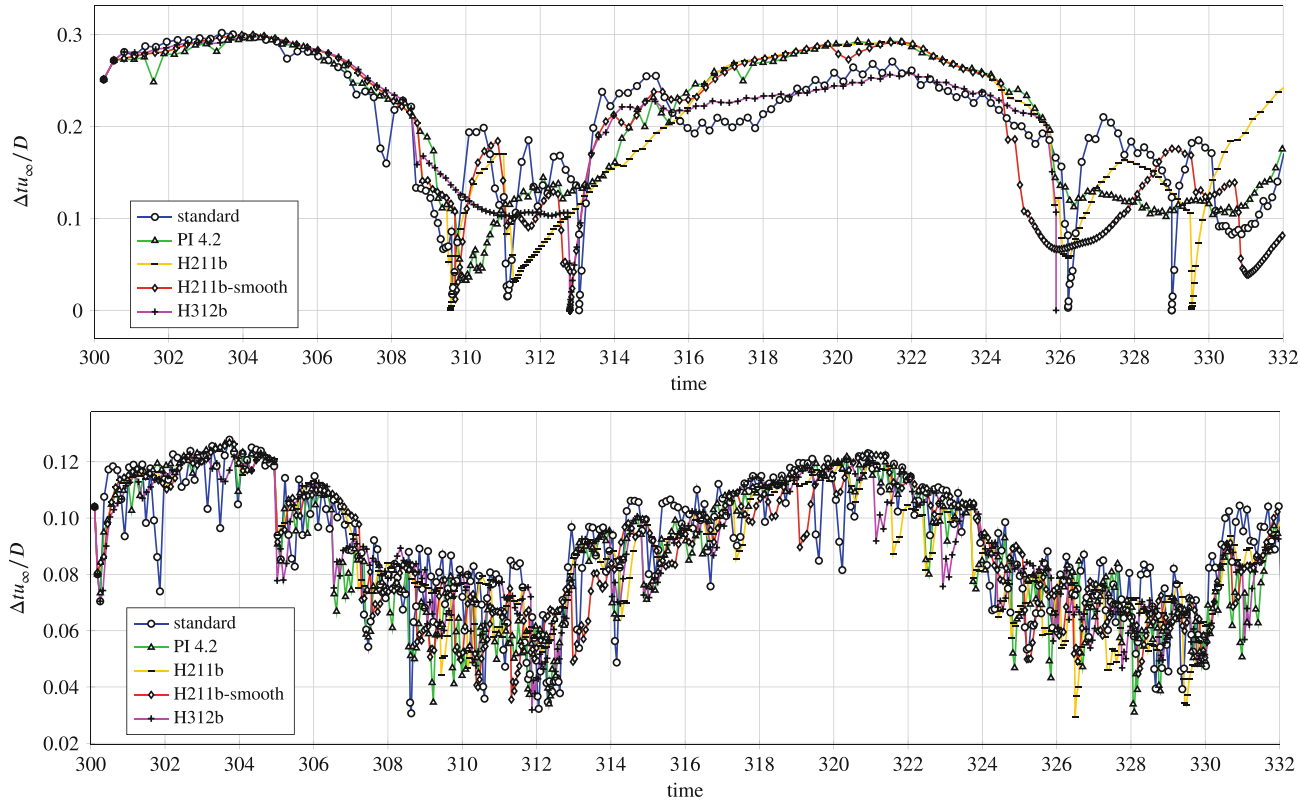

FIGURE 10 Cylinder $Re = 3900$. Time-step $\Delta tu_\infty/D$ evolution with different controller in the compressible case, ROS3PL scheme with $\|err_p\| \sim 10^{-4}$ (top) and $\|err_p\| \sim 10^{-5}$ (bottom), $tol_{system} = 10^{-14}$, and discontinuous Galerkin (DG)-$\mathbb{P}^5$ solution approximation

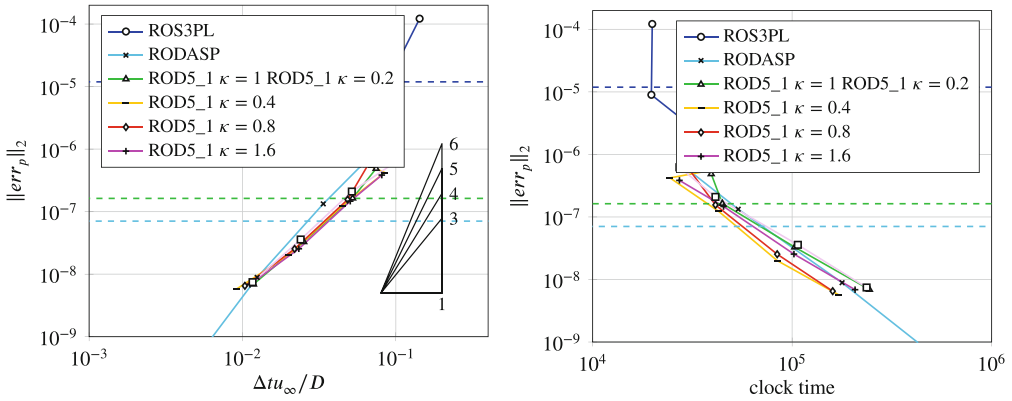

FIGURE 11 Cylinder $Re = 3900$. L^2 norm of the pressure error ($\|err_p\|_2$) as a function of the time-averaged time-step $\Delta tu_\infty/D$ and the clock time with different time integration schemes in the compressible case, H211b-smooth controller with $tol_{system} = 10^{-14}$, and discontinuous Galerkin (DG)-$\mathbb{P}^5$ solution approximation. The horizontal dashed lines represent the limit of stability of the schemes with constant time-steps, that is, without the adaptive time-step strategy

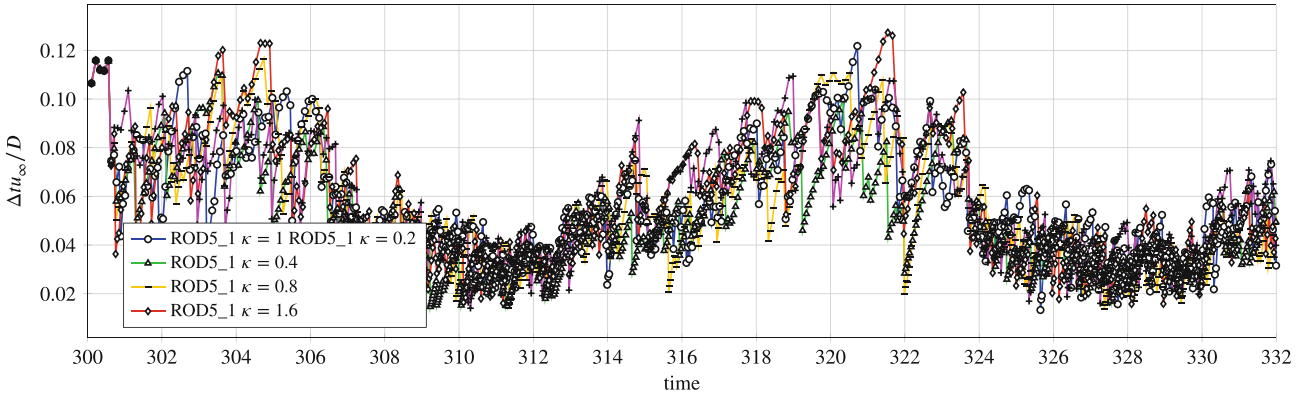

FIGURE 12 Cylinder $Re = 3900$. Time-step $\Delta tu_\infty/D$ evolution with different κ values of H211b-smooth controller in the compressible case, ROD5_1 scheme with $\|err_p\| \sim 2 \times 10^{-7}$, $tol_{system} = 10^{-14}$, and discontinuous Galerkin (DG)-$\mathbb{P}^5$ solution approximation

between simulation with and without adaptive strategy. This behavior suggests that the use of the time-step adaptation strategy in this zone is useless, and, in general, is characterized by the absence of rejected time-steps. The adaptation algorithm becomes useful in the near-stability zone, where a simulation with a fixed time-step is unstable. Moreover, the adaptation strategy allows to go beyond the near-stability zone. Table 10 summarizes the performance of the different schemes and strategies in the near-stability zone, in terms of the time-averaged time-step $\Delta tu_\infty/D$, the L^2 norm of the pressure error $\|err_p\|_2$ and the clock time. In particular, the increased robustness of the time integration for the use of a time-step adaptation strategy is evident. Only in some cases, the stability improvement corresponds to a decay of the computational efficiency, as suggested by the change of the curve slope. H211b is the controller that guarantees the higher increase of the near-stability zone, which is up to one order of magnitude for the schemes with higher number of stages. ROS3PL shows a huge increase of the near-stability zone with a reduction or a negligible increment of the computing time, while ROD5_1, even increasing the near-stability zone, shows the lower values of $\Delta_{\|err_p\|_2}$. The different schemes are also compared with the same controller, that is, the H211b-smooth controller, and figure 11 shows the performance of the schemes in terms of the L^2 norm of the pressure error $\|err_p\|_2$ and the clock time. Different values of the κ parameter are also considered to investigated its influence on the computing time. The performance of the schemes with the adaptive time-step strategy (solid line) has been compared with the performance of the simulations without adaptation (dashed lines). As expected, high-order time integration schemes perform better for increasing temporal accuracy, that is, with lower time-step. ROS3PL shows the best results for relative high-levels of the error, while ROD5_1 for lower levels. $\kappa = 0.4$ represents the best compromise between the reducing of the computational cost and the increasing of the robustness.

TABLE 10 Cylinder $Re = 3900$. Comparison between the near-stability zone, in terms of the time-averaged time-step $\Delta tu_\infty/D$, L^2 norm of the pressure error $\|err_p\|_2$, and the clock time, for ROS3PL, RODASP, and ROD5_1 schemes and different controllers, in the compressible case $tol_{System} = 10^{-16}$ and DG-$\mathbb{P}^6$ solution approximation. The limit of stability without the adaptive time-step strategy of ROS3PL is $\{\|err_p\|_2, \text{clock time}\} = \{1.19\text{E}-05, 1.85\text{E}+04\}$, of RODASP is $\{7.05\text{E}-08, 5.74\text{E}+04\}$, and of ROD5_1 is $\{1.63\text{E}-07, 4.77\text{E}+04\}$

Scheme	Controller	$\Delta tu_\infty/D$	$\|err_p\|_2$	Clock time	$\Delta_{\|err_p\|_2}$ [%]	$\Delta_{\text{clock time}}$ [%]
ROS3PL	Standard	1.68E-01	1.13E-04	1.13E+04	849.58	−38.92
	PI 4.2	1.62E-01	1.96E-04	1.42E+04	1547.06	−23.24
	H211b	2.60E-01	3.67E-04	2.01E+04	2984.03	8.65
	H211b-smooth	1.43E-01	1.22E-04	1.99E+04	925.21	7.57
	H312b	1.83E-01	2.05E-04	1.37E+04	1622.69	−25.95
RODASP	Standard	7.28E-02	8.43E-07	3.69E+04	1095.74	−35.71
	PI 4.2	4.22E-02	8.79E-07	4.46E+04	1146.81	−22.30
	H211b	9.31E-02	1.82E-06	2.63E+04	2481.56	−54.18
	H211b-smooth	6.05E-02	5.63E-07	3.02E+04	698.58	−47.39
	H312b	8.31E-02	8.38E-07	2.31E+04	1088.65	−59.76
ROD5_1	Standard	5.46E-02	2.11E-07	4.74E+04	29.45	−0.63
	PI 4.2	9.34E-02	4.87E-07	2.62E+04	198.77	−45.07
	H211b	8.18E-02	4.04E-07	3.43E+04	147.85	−28.09
	H211b-smooth	7.44E-02	4.88E-07	3.93E+04	199.39	−17.61
	H312b	7.19E-02	3.33E-07	4.35E+04	104.29	−8.81

Abbreviation: DG, discontinuous Galerkin.

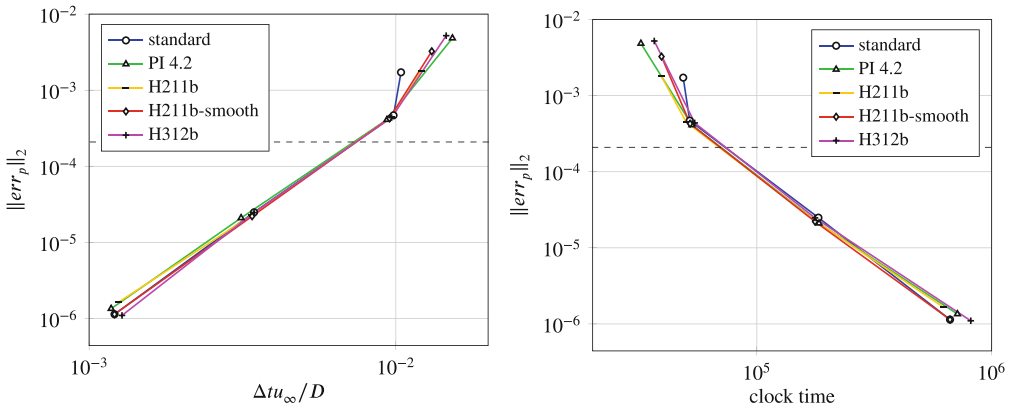

FIGURE 13 Cylinder $Re = 3900$. L^2 norm of the pressure error ($\|err_p\|_2$) as a function of the time-averaged time-step $\Delta tu_\infty/D$ and the clock time [wu] with different controller in the incompressible case, ROS3PL scheme with $tol_{system} = 10^{-14}$ and discontinuous Galerkin (DG)-$\mathbb{P}^5$ solution approximation. The horizontal dashed line represents the limit of stability of the scheme with constant time-steps, that is, without the adaptive time-step strategy

For the incompressible case figure 13 shows the performance of the different controller in terms of the L^2 norm of the pressure error $\|err_p\|_2$ and the clock time, while Figure 14 shows the evolution of the adaptive time-step $\Delta tu_\infty/D$ for the ROS3PL scheme. Similarly to the compressible case, decreasing the time-step the effect of the adaptation strategy is negligible, and the fixed time-step can be used. Table 11 summarizes the performance of the different schemes and strategies in the near-stability zone. Only the stability improvement of peer4 corresponds to a decay of the computational efficiency. H211b-smooth and H312b are the controller that guarantee the higher increase of the near-stability zone. Peer schemes show the higher increase of the near-stability zone with a reduction or a negligible increment of the computing time.

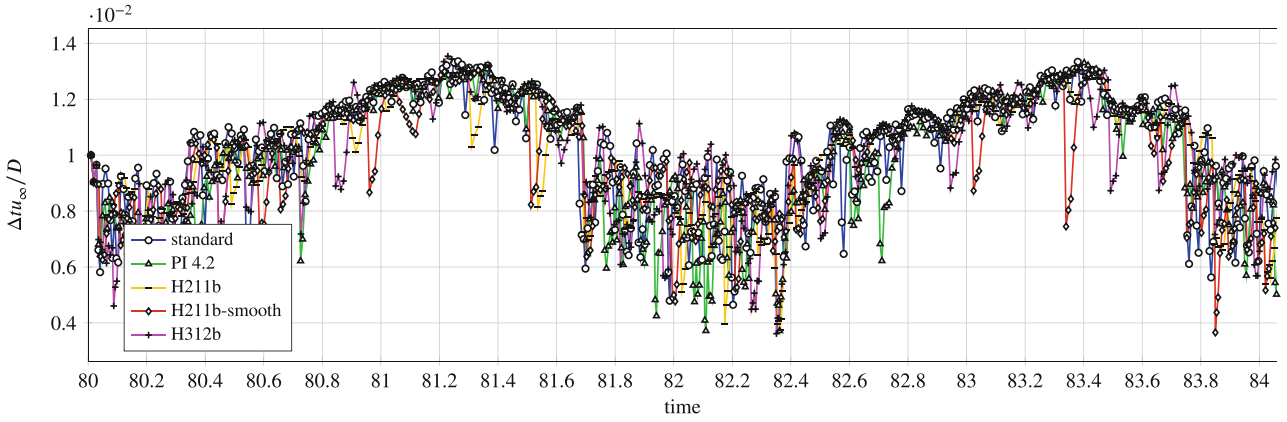

FIGURE 14 Cylinder $Re = 3900$. Time-step $\Delta tu_\infty/D$ evolution with different controllers in the incompressible case, ROS3PL scheme with $\|err_p\| \sim 10^{-4}$, $tol_{system} = 10^{-14}$, and discontinuous Galerkin (DG)-$\mathbb{P}^5$ solution approximation

TABLE 11 Cylinder $Re = 3900$. Comparison between the near-stability zone, in terms of the time-averaged time-step $\Delta tu_\infty/D$, L^2 norm of the pressure error $\|err_p\|_2$ and the clock time, for the different schemes and controllers in the incompressible case, $tol_{System} = 10^{-16}$ and DG-$\mathbb{P}^6$ solution approximation. The limit of stability without the adaptive time-step strategy of ROS3PL is $\{\|err_p\|_2, \text{clock time}\} = \{2.09\text{E}-04, 1.59\text{E}+05\}$, of RODASP is $\{2.08\text{E}-04, 4.26\text{E}+05\}$, of ROD5_1 is $\{2.36\text{E}-04, 3.62\text{E}+05\}$ and of peer3, peer4, and peer5 respectively $\{7.86\text{E}-06, 1.06\text{E}+05\}$, $\{5.31\text{E}-06, 6.72\text{E}+04\}$, and $\{6.96\text{E}-06, 1.33\text{E}+05\}$

Scheme	Controller	$\Delta tu_\infty/D$	$\|err_p\|_2$	Clock time	$\Delta_{\|err_p\|_2}$ [%]	$\Delta_{\text{clock time}}$ [%]
ROS3PL	Standard	1.72E-03	1.04E-02	4.86E+04	4871.40	−69.52
	PI 4.2	4.83E-03	1.53E-02	3.21E+04	7213.70	−79.87
	H211b	1.79E-03	1.21E-02	3.93E+04	5684.03	−75.35
	H211b-smooth	3.25E-03	1.31E-02	3.93E+04	6162.05	−75.35
	H312b	5.21E-03	1.46E-02	3.66E+04	6879.08	−77.04
RODASP	H211b	1.75E-05	9.40E-03	1.03E+05	4411.56	−75.82
ROD5_1	H211b	9.82E-05	5.78E-03	1.38E+05	2345.54	−61.91
peer3	H211b	2.29E-03	3.99E-03	4.57E+04	50678.96	−56.75
peer4	H211b	1.22E-04	5.08E-03	7.39E+04	95634.53	9.94
peer5	H211b	3.81E-05	5.99E-03	1.02E+05	85976.90	−23.39

In general, all the schemes show a higher increase of the robustness with the adaptive time-step strategy in comparison with the compressible case. Figure 15 compares different schemes with the same controller, that is, the H211b controller, in terms of the L^2 norm of the pressure error $\|err_p\|_2$ and the clock time. The performance of the schemes with the adaptive time-step strategy (solid line) has been compared with the performance of the simulations without adaptation (dashed lines). ROS3PL shows the best results for relative high-levels of the error in comparison with peer3, while RODASP and peer5 outperform ROD5_1 for lower levels. In fact, ROD5_1 loses the efficiency demonstrated for compressible flows, probably for the higher cost in the resolution of the intermediate solutions, while peers increase their efficiency for a faster resolution of the linear system. For stiff problems, such as turbulent flows modeled by the RANS equations, the convergence order can not be verified exactly as for laminar test cases. The convergence order is approximately verified for the one-step Rosenbrock schemes ($q_{ROS3PL} = 2.8$, $q_{RODASP} = 4.3$, and $q_{ROD5_1} = 5.4$) while is lower for the peer schemes ($q_{peer3} = 3.3$, $q_{peer4} = 3.1$, and $q_{peer5} = 1.8$).

6.2 | Turbulent flow around a circular cylinder at $Re = 140{,}000$

To investigate the performance of the controller and the schemes in a problem with increasing stiffness, the turbulent flow around a circular cylinder at high sub-critical Reynolds number $Re = 140{,}000$, based on the cylinder diameter and

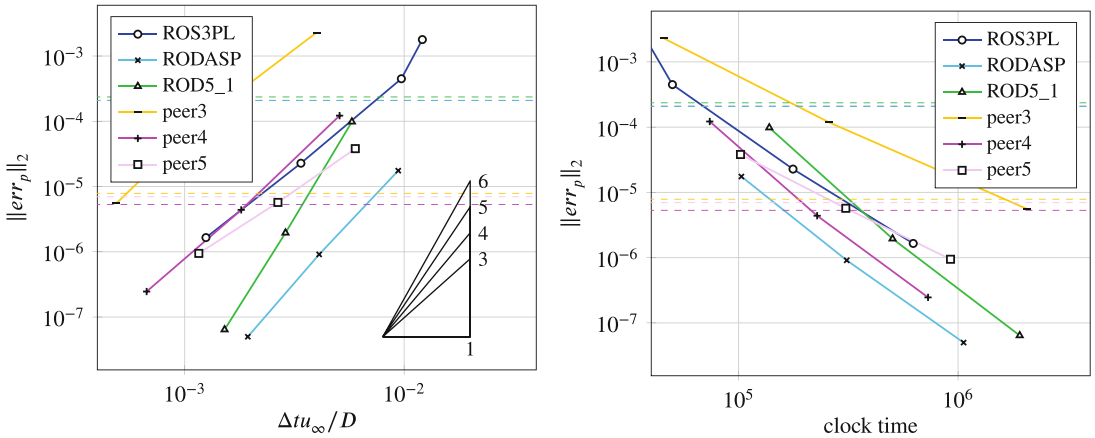

FIGURE 15 Cylinder $Re = 3900$. L^2 norm of the pressure error ($\|err_p\|_2$) as a function of the time-averaged time-step $\Delta t u_\infty / D$ and the clock time with different time integration schemes in the incompressible case, H211b controller with $tol_{system} = 10^{-14}$ and discontinuous Galerkin (DG)-$\mathbb{P}^5$ solution approximation. The horizontal dashed lines represent the limit of stability of the schemes with constant time-steps, that is, without the adaptive time-step strategy

the freestream quantities, is here considered. The Mach number is set to $M = 0.1$ to consider the flow essentially incompressible. The flow is near the critical Reynolds number and for this reason is a challenging problem of fluid mechanics, both from an experimental and a numerical point of view. As in the previous case, the boundary layer is still laminar until the separation, but the laminar-turbulent transition of the shear layer takes place very shortly after separation, with the creation of Kelvin–Helmholtz instabilities with the break-up of the shear layer and an asymmetric Von Kármán vortex shedding. For slightly higher values of the Reynolds number, that is, around $Re = 200{,}000 - 300{,}000$ for the circular cylinder, the (attached) boundary layer becomes turbulent, the Strouhal number increases, and the well-known drag crisis is observed.

The success of a mathematical model is critically dependent on the ability to predict the location of the separation and the laminar-turbulent transition, in fact the location of these phenomena is determined by the magnitude of the Reynolds number and near the critical values separation and transition happen very close one each other. It is likely that the well recognized limitations of turbulence models to deal with turbulence onset cause the premature occurrence of the break-down to high intensity turbulence with the laminar-turbulent transition, which happens in the (attached) boundary layer. Shur et al.[37] introduces the trip-less turbulent separation (TS) case, in comparison with the laminar separation (LS) case, in order to gives RANS and turbulence models control over the phenomenon. In this case reference data are those obtained at higher Reynolds number, that is, $Re > 200{,}000$,[38-41] in order to have a comparison with acceptable error margins.

Literature shows experimental works on the flow around a circular cylinder in critical flow state, however as the flow at these high-Reynolds numbers is very sensitive to free-stream turbulent fluctuations, surface roughness and in general boundary conditions, the scattering of the measurements is very high. A limited number of high-accuracy simulations LES, or implicit LES, and hybrid RANS–LES were carried out during the last two decades. Frohlich et al.,[42,43] Breuer[36] performed LES with different subgrid scale model with studies on the influence of the parameter of the subgrid scale model on the results. More significant for this work are the simulations performed with hybrid RANS–LES methods by Travin et al.,[44] with SA-DES, and Islam and Thornber,[45] with a RANS–ILES approach. Travin et al.[44] spotlight the different behavior of the turbulence model in the near-wall region with the distinction between LS and TS, in fact the Spalart–Allmaras turbulence model allows to describe both laminar, by imposing a zero eddy viscosity inflow until separation, and turbulent separation. This is acknowledged to be the best way to match the experimental results and a LES-like behavior of this case also with a turbulence model. The $k - \omega$ model, here used, differs from the Spalart–Allmaras model and no numerical trigger on the free-stream condition allows to obtain a LES-like behavior of the near-wall region.

The mesh has 4343 hybrid elements, triangles, and quadrilaterals, with quadratic edges and the solution is a very accurate DG-$\mathbb{P}^5$ with 91,203 DOFs per equation. Figure 16 shows the instantaneous x-component velocity and turbulent intensity contours.

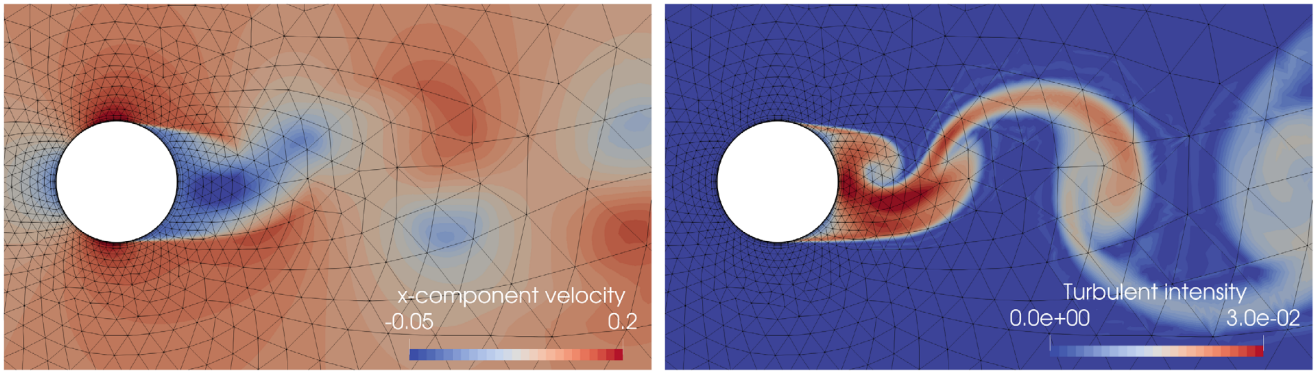

FIGURE 16 Cylinder $Re = 140{,}000$. Instantaneous x-component velocity (left) and turbulent intensity (right) contours, discontinuous Galerkin (DG)-$\mathbb{P}^5$ solution approximation

TABLE 12 Cylinder $Re = 140{,}000$. Comparison of the root-mean-square lift coefficient $c_{L\,rms}$, the time-averaged drag coefficient c_D, the Strouhal number St, the time-averaged separation angles θ_{sep}, the time-averaged base suction coefficient $-c_{p\,b}$, the time-averaged peak of the stream-wise velocity in the wake $-u_{min}/u_{\inf}$, and the time-averaged recirculation zone length L_r/D, between literature and results

	c_D	$c_{L\,rms}$	St	$-c_{p\,b}$	L_r/D	$-u_{min}/u_\infty$	θ_{sep}
Cantwell and Coles exp.[46]	1.237	—	0.179	1.21	0.44	—	—
Roshko exp.[38]	0.7	—	0.27	0.8	—	—	—
Islam and Thornber RANS-ILES[45]	0.869	—	0.271	0.767	1.26	0.367	96.38°
Frohlich et al.LES[42]	1.147	—	0.217	1.33	0.42	0.145	79°
Travin et al. SA-DES LS8[44]	1.08	0.29	0.21	1.04	1.1	0.261	77°
Travin et al. SA-DES TS5[44]	0.65	0.06	0.28	0.70	1.4	—	93°
Moussaed et al. RANS[47]	0.76	0.43	0.27	0.85	0.67	—	—
RANS DG-$\mathbb{P}^5$	0.75	0.44	0.27	0.86	0.72	—	91°

Abbreviations: DG, discontinuous Galerkin; RANS, reynolds-averaged Navier–Stokes; LES large eddy simulation.

The Strouhal number $St = 0.271$ is in agreement with the experimental data, while the time-averaged drag coefficient $c_D = 0.751$ is slightly different, but similar to the other two-dimensional RANS numerical results. Table 12 summarizes the results in comparison with experiment and other numerical results. In particular, the root-mean-square lift coefficient $c_{L\,rms}$, the time-averaged drag coefficient c_D, the Strouhal number St, the time-averaged separation angles θ_{sep}, the time-averaged base suction coefficient $-c_{p\,b}$, the time-averaged peak of the stream-wise velocity in the wake $-u_{min}/u_{\inf}$, and the time-averaged recirculation zone length L_r/D are reported. Figure 17 shows the time-averaged pressure c_p and skin friction c_f coefficient distribution on the cylinder in comparison with experimental and other numerical results.

Figure 18 shows the performance of the different controller in terms of the L^2 norm of the pressure error $\|err_p\|_2$ and the clock time, while Figure 19 shows the evolution of the adaptive time-step $\Delta t u_\infty/D$ with ROS3PL and different levels of error. The behavior of the previous case can be observed also here, that is, for small time-step the adaptation strategy is useless. The adaptation algorithm becomes useful around the near-stability zone, where the simulations with a fixed time-step are unstable. Table 13 summarizes the performance of the different schemes and strategies in the near-stability zone in terms of the time-averaged time-step $\Delta t u_\infty/D$, the L^2 norm of the pressure error $\|err_p\|_2$, and the clock time. H211b-smooth and H312b are the best controller, that is, able to guarantee the higher increase of robustness in the near-stability zone. Figure 19 compares the effect of different controllers on the ROS3PL scheme. In particular, the smooth function for the H211b controller provides a smooth change of the time-step, while sharp variations are evident for the standard controller. Moreover, the controllers do not show appreciable differences for higher accuracy and lower averaged time-step.

Figure 20 compares different schemes with the H211b controller in terms of the L^2 norm of the pressure error $\|err_p\|_2$ and the clock time. The performance of the schemes with the adaptive time-step strategy (solid line) has been compared

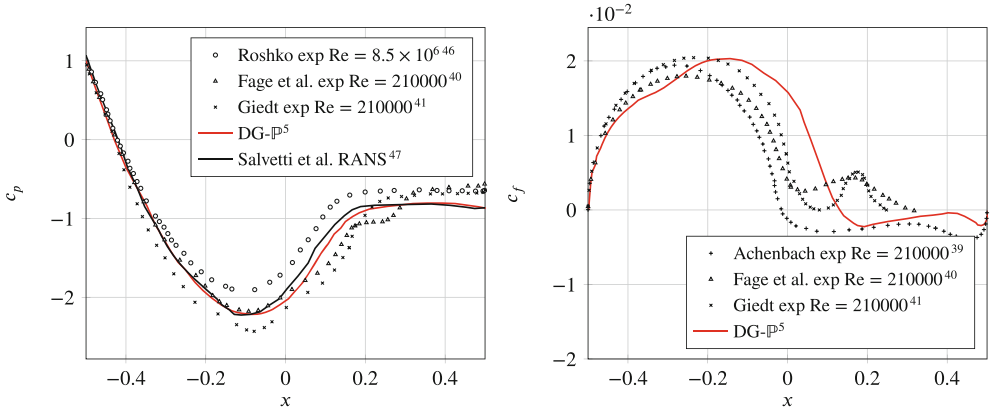

FIGURE 17 Cylinder $Re = 140{,}000$. Time-averaged pressure c_p (left) and skin friction c_f (right) coefficient distribution on the cylinder, discontinuous Galerkin (DG)-$\mathbb{P}^5$ solution approximation

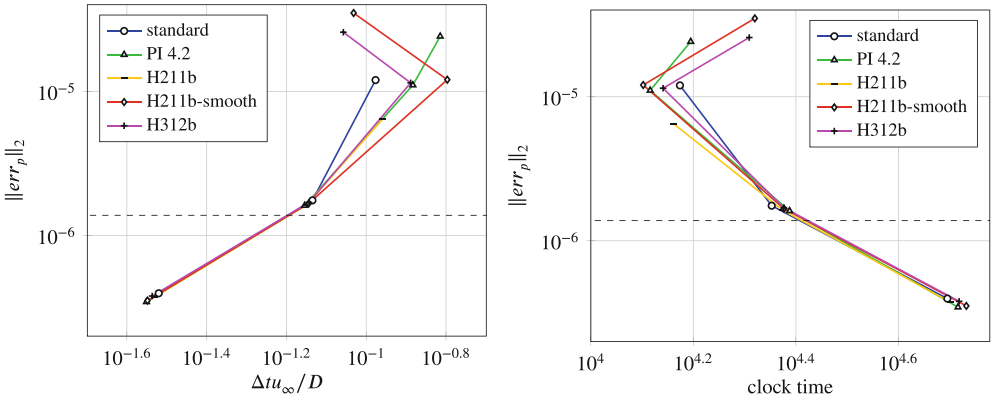

FIGURE 18 Cylinder $Re = 140{,}000$. L^2 norm of the pressure error ($\|err_p\|_2$) as a function of the rime-averaged time-step $\Delta t u_\infty / D$ and the clock time with different controller, ROS3PL scheme with $tol_{system} = 10^{-14}$ and discontinuous Galerkin (DG)-$\mathbb{P}^5$ solution approximation. The horizontal dashed line represent the limit of stability of the scheme with constant time-steps, that is, without the adaptive time-step strategy

with simulations without adaptation (dashed lines). Similarly to the previous compressible case, ROS3PL is the most efficient for lower accuracy, while ROD5_1 for higher accuracy.

6.3 | Turbulent flow around a tandem cylinders at $Re = 166{,}000$

The compressible turbulent flow around a tandem cylinders at high sub-critical Reynolds number $Re = 166{,}000$, based on the cylinder diameter and the freestream quantities, and a distance $L/D = 3.7$ is here considered. The Mach number is set to $M = 0.1$ to consider the flow essentially incompressible. The mesh has 5558 hybrid elements, triangles, and quadrilaterals, with quadratic edges and the solution is a DG-$\mathbb{P}^5$ with 116,718 DOFs per equation. Figure 21 shows the instantaneous x-component velocity and turbulent intensity contours.

Literature is very poor about numerical and experimental results of turbulent flows around a tandem of cylinders. Although the case of a tandem cylinder configuration has been considered before, nearly all of the past studies were restricted to the low Reynolds number flow regime, for example, $Re = 100$. According to Khorrami et al.,[48] different flow regimes can be observed in such flows. The three most prominent correspond to short, intermediate, and large separation distances between the cylinders. In the case of short separations, that is, $L/D < 2.4$, the two cylinders behave as a single bluff body with vortex shedding occurring at the rear cylinder only. For large separation distances, the flow field approaches that of isolated single cylinders. At intermediate separation distances, the flow is bi-stable, switching intermittently between the flow states corresponding to short and large separation distances, where this critical flow regime

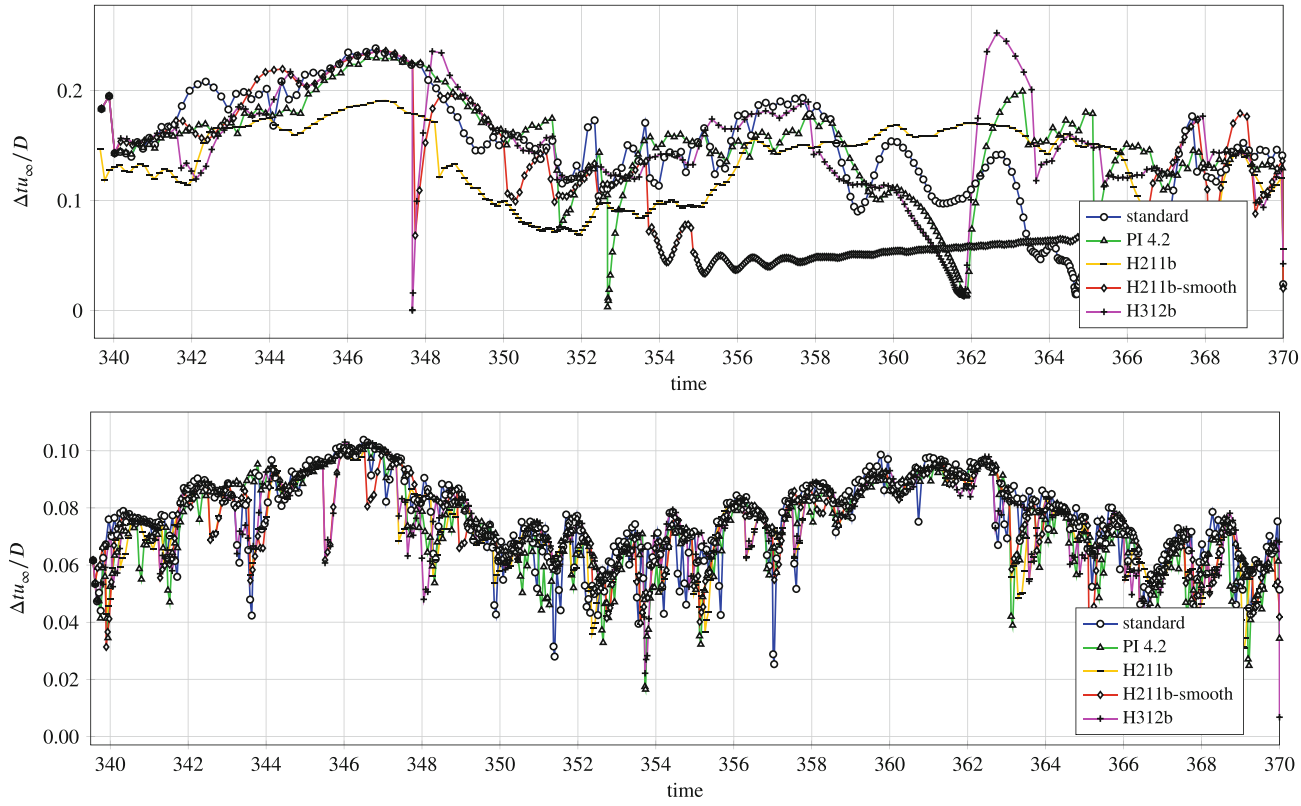

FIGURE 19 Cylinder $Re = 140{,}000$. Time-step $\Delta tu_\infty/D$ evolution with different controller, ROS3PL scheme with $\|err_p\| \sim 10^{-5}$ (top) and $\|err_p\| \sim 10^{-6}$ (bottom), $tol_{system} = 10^{-14}$, and discontinuous Galerkin (DG)-$\mathbb{P}^5$ solution approximation

TABLE 13 Cylinder $Re = 140{,}000$. Comparison between the near-stability zone, in terms of the time-averaged time-step $\Delta tu_\infty/D$, L^2 norm of the pressure error $\|err_p\|_2$ and the clock time, for the different schemes and controllers, $tol_{System} = 10^{-16}$, and DG-$\mathbb{P}^5$ solution approximation. The limit of stability without the adaptive time-step strategy of ROS3PL is $\{\|err_p\|_2, \text{clock time}\} = \{1.38\text{E}-06, 1.65\text{E}+04\}$, of RODASP is $\{7.45\text{E}-08, 2.95\text{E}+04\}$, and of ROD5_1 is $\{56.24\text{E}-08, 2.95\text{E}+04\}$

Scheme	Controller	$\Delta tu_\infty/D$	$\|err_p\|_2$	Clock time	$\Delta_{\|err_p\|_2}$ [%]	$\Delta_{\text{clock time}}$ [%]
ROS3PL	Standard	1.05E-01	1.19E-05	1.49E+04	3416.51	−9.93
	PI 4.2	1.53E-01	2.41E-05	1.56E+04	7021.67	−5.70
	H211b	1.10E-01	6.46E-06	1.45E+04	1808.96	−12.35
	H211b-smooth	9.29E-02	3.50E-05	2.08E+04	10242.67	25.73
	H312b	8.76E-02	2.57E-05	2.03E+04	7494.48	22.71
RODASP	H211b-smooth	8.59E-02	6.32E-07	2.52E+04	879.19	−14.58
ROD5_1	H211b-smooth	8.48E-02	3.61E-07	2.71E+04	2802.42	−8.03

is the most difficult to simulate. The separation distance here considered represents the second type of flow. Figure 22 shows the time-averaged pressure coefficient c_p distribution for the front (left) and the rear (right) cylinder, in comparison with the experimental and the numerical results by Khorrami et al.[48]

Figure 23 shows the performance of the different controller in terms of the L^2 norm of the pressure error $\|err_p\|_2$ and the clock time, while Figure 24 shows the evolution of the adaptive time-step $\Delta tu_\infty/D$ for the ROS3PL and different levels of error. The same behavior found in the single cylinder, that is, both for $Re = 3900$ and $Re = 140{,}000$, can be observed also in this case, that is, the adaptation algorithm becomes useful around the near-stability zone, where the simulations with a fixed time-step are unstable. Figure 24 shows also the comparison between H211b and H211b-smooth controllers and between a higher-order controller, as H312b, and a lower-order controller, as standard. The influence of

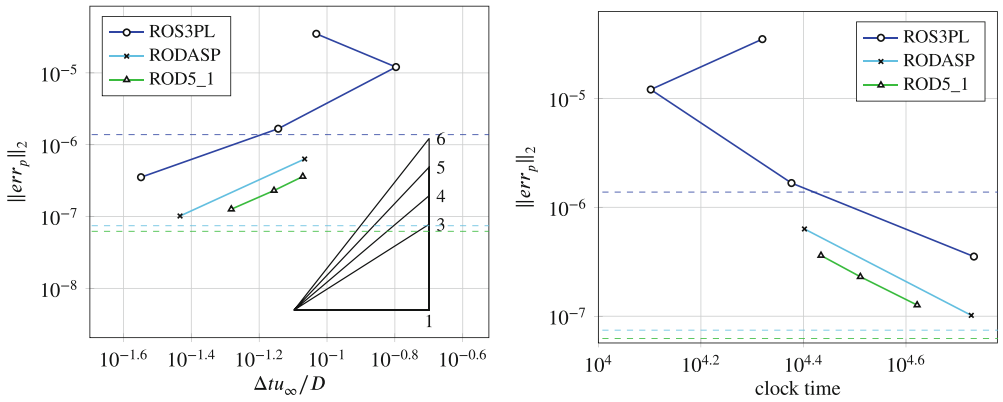

FIGURE 20 Cylinder $Re = 140{,}000$. L^2 norm of the pressure error ($\|err_p\|_2$) as a function of the time-averaged time-step $\Delta t u_\infty / D$ and the clock time with different time integration schemes, H211b-smooth controller with $tol_{system} = 10^{-14}$, and discontinuous Galerkin (DG)-$\mathbb{P}^5$ solution approximation. The horizontal dashed lines represent the limit of stability of the schemes with constant time-steps, that is, without the adaptive time-step strategy

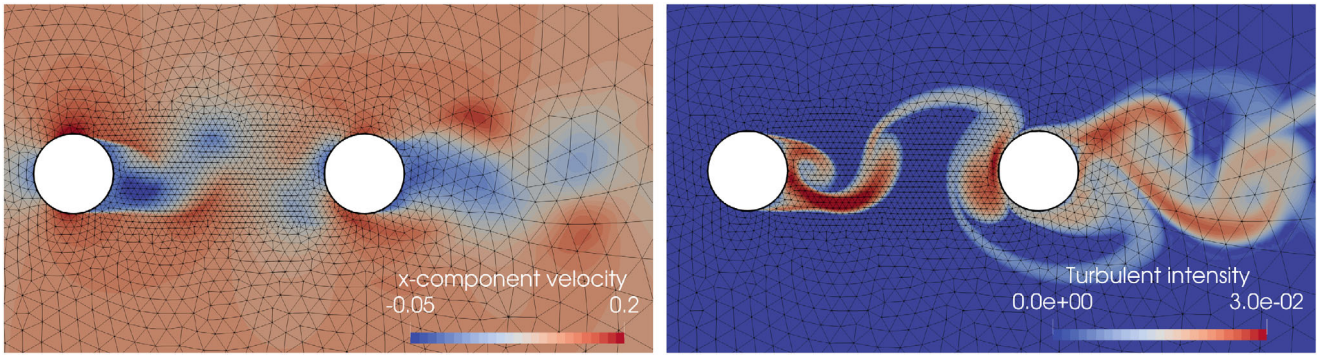

FIGURE 21 Tandem cylinders $Re = 166{,}000$. Instantaneous x-component velocity (left) and turbulent intensity (right) contours, discontinuous Galerkin (DG)-$\mathbb{P}^5$ solution approximation.

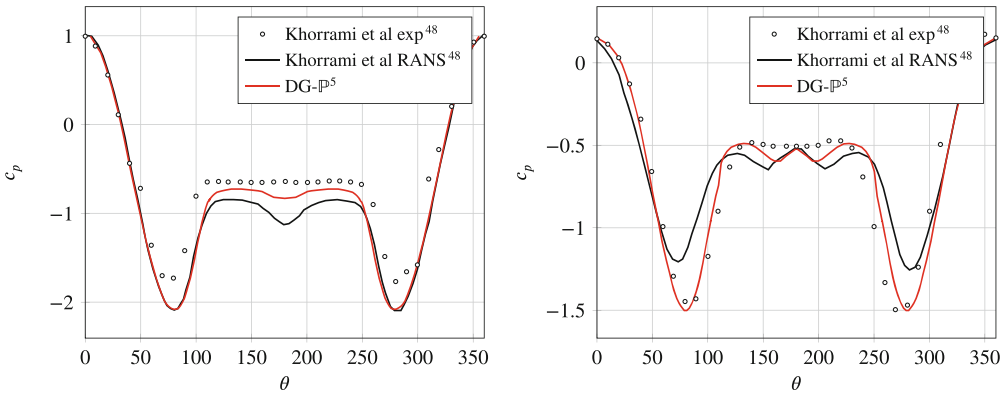

FIGURE 22 Tandem cylinders $Re = 166{,}000$. Time-averaged pressure coefficient c_p distribution on the front (left) and rear (right) cylinder, discontinuous Galerkin (DG)-$\mathbb{P}^5$ solution approximation

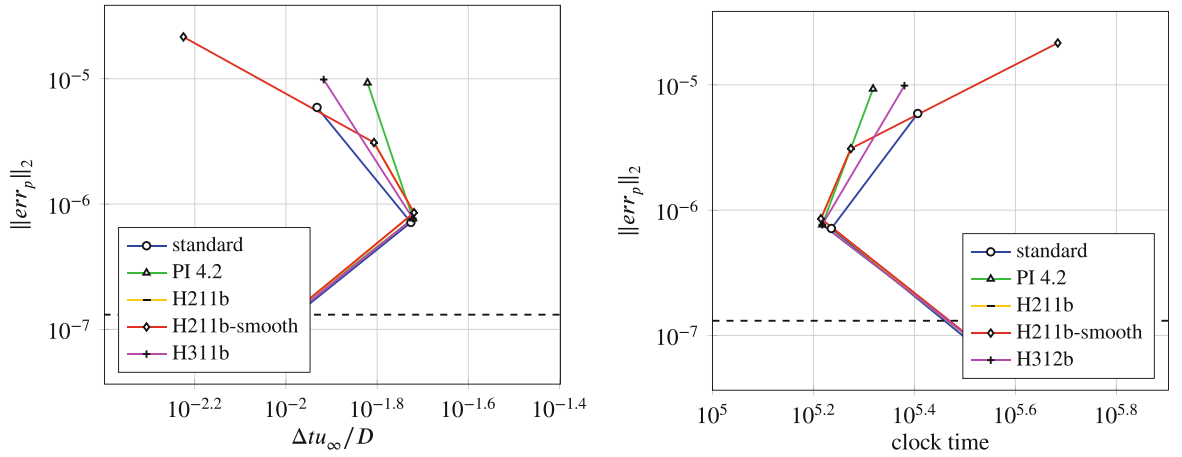

FIGURE 23 Tandem cylinders $Re = 166{,}000$. L^2 norm of the pressure error ($\|err_p\|_2$) as a function of the average time-step $\Delta tu_\infty / D$ (left) and the clock time (right) with different controller, ROS3PL scheme with $tol_{system} = 10^{-14}$, and discontinuous Galerkin (DG)-$\mathbb{P}^5$ solution approximation. The horizontal dashed line represents the limit of stability of the scheme with constant time-steps, that is, without the adaptive time-step strategy

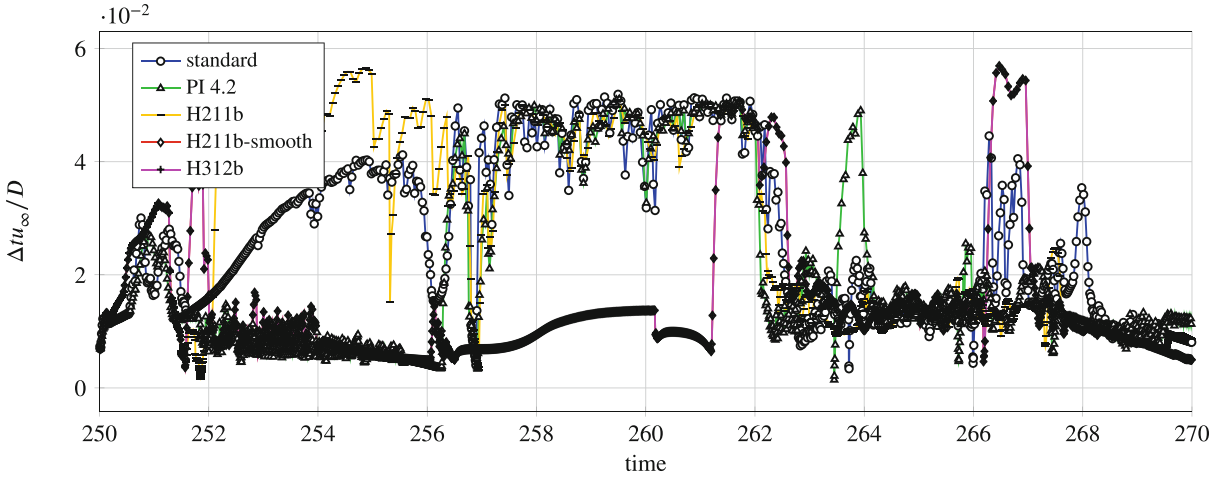

FIGURE 24 Tandem cylinders $Re = 166{,}000$. Time-step $\Delta tu_\infty / D$ evolution with different controller, ROS3PL scheme with $TOL = 10^{-6}$, $tol_{system} = 10^{-14}$, and discontinuous Galerkin (DG)-$\mathbb{P}^5$ solution approximation

the smooth function of the H211b controller and the order of the controllers is increasingly high with the complexity and the stiffness of the case, an higher order of the controller can be viewed as a smooth introduced in the behavior of the controller. Table 14 summarizes the performance of the different schemes and strategies in the near-stability zone in terms of the time-averaged time-step $\Delta tu_\infty / D$, the L^2 norm of the pressure error $\|err_p\|_2$ and the clock time. H211b-smooth and H312b are the best controller, which guarantee the higher increase of robustness in the near-stability zone. The stability improvement corresponds to a decay of the computational efficiency for all the schemes and the controller.

Figure 25 compares different schemes with the H211b-smooth controller in terms of the pressure error $\|err_p\|_2$ and the clock time. The performance of the schemes with the adaptive time-step strategy (solid line) has been compared with simulations without adaptation strategy (dashed lines). Similarly to the previous compressible case, ROS3PL is the most efficient for lower accuracy, while ROD5_1 for higher accuracy.

Finally, the influence of the correction factor η, defined in Equation (5), and the maximum allowed time-step Δt_{limit}, defined in Equation (5), is investigated for the ROS3PL scheme and H211b controller. Figures 26 and 27 show the L^2 norm of the pressure error $\|err_p\|_2$ functions of the time-averaged time-step $\Delta tu_\infty / D$ and the clock time with different correction factors and maximum allowed time-steps. Figure 28 shows the evolution of the adaptive time-step $\Delta tu_\infty / D$

TABLE 14 Tandem cylinders $Re = 166{,}000$. Comparison between the near-stability zone, in terms of the time-averaged time-step $\Delta tu_\infty/D$, L^2 norm of the pressure error $\|err_p\|_2$ and the clock time, for the different schemes and controllers, $tol_{System} = 10^{-16}$, and DG-$\mathbb{P}^6$ solution approximation. The limit of stability without the adaptive time-step strategy of ROS3PL is $\{\|err_p\|_2, \text{clock time}\} = \{1.38\text{E}-06, 1.65\text{E}+04\}$, of RODASP is $\{7.45\text{E}-08, 2.95\text{E}+04\}$, and of ROD5_1 is $\{5.62\text{E}-08, 2.95\text{E}+04\}$

Scheme	Controller	$\Delta tu_\infty/D$	$\|err_p\|_2$	Clock time	$\Delta_{\|err_p\|_2}$ [%]	$\Delta_{\text{clock time}}$ [%]
ROS3PL	Standard	1.17E-02	5.91E-06	2.55E+05	4411.45	155.25
	PI 4.2	1.51E-02	9.29E-06	2.08E+05	6991.60	108.40
	H211b	1.56E-02	3.10E-06	1.88E+05	2266.41	88.65
	H211b-smooth	5.96E-03	2.16E-05	4.83E+05	16388.55	383.35
	H312b	1.21E-02	9.86E-06	2.40E+05	7426.72	140.42
RODASP	H211b-smooth	7.97E-03	6.76E-06	4.11E+05	56233.33	311.11
ROD5_1	H211b-smooth	2.66E-02	9.18E-08	1.55E+05	1695.28	55.19

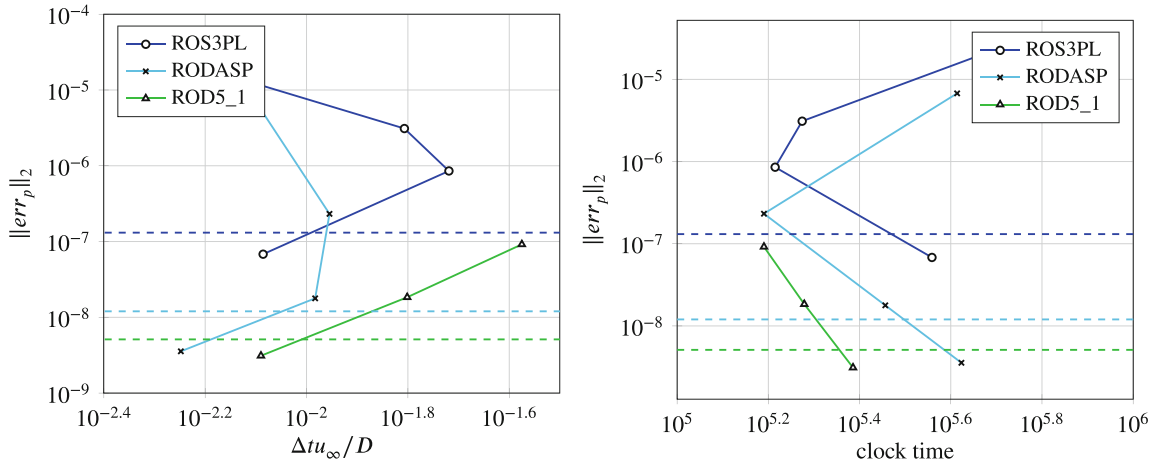

FIGURE 25 Tandem cylinders $Re = 166{,}000$. L^2 norm of the pressure error ($\|err_p\|_2$) as a function of the time-averaged time-step $\Delta tu_\infty/D$ (left) and the clock time [wu] (right) with different time integration schemes, H211b-smooth controller, $tol_{system} = 10^{-14}$, and discontinuous Galerkin (DG)-$\mathbb{P}^5$ solution approximation. The horizontal dashed lines represent the limit of stability of the schemes with constant time-steps, that is, without the adaptive time-step strategy

with ROS3PL, H211b controller, and different maximum allowed time-steps. The robustness and the efficiency of the controllers are substantially improved by limiting the maximum possible time-step, while they are not affected by the bound of the maximum increase/reduction.

6.4 | Unsteady turbulent flow through a VAWT

Finally, in order to prove the effectiveness of the proposed adaptive high-order time integration, the unsteady turbulent flow through a VAWT is simulated. The Mach number is set to $M = 0.1$ to consider the flow essentially incompressible. This case is characterized by strongly unsteady flow features with a wide range of spatial and temporal scales over (very) long time periods.

The results of previous cases show that peer5, for incompressible equations, and ROD5_1, both for compressible and incompressible equations, are the best schemes for very accurate unsteady solutions, while for lower accuracy ROS3PL should be preferred. Considering that the level of accuracy ensured by ROS3PL is sufficient for the current investigation, the ROS3PL scheme with H211b-smooth controller is used. The smooth limiter function is applied to improve the robustness of the H211b controller, limiting the variation of the time-step.

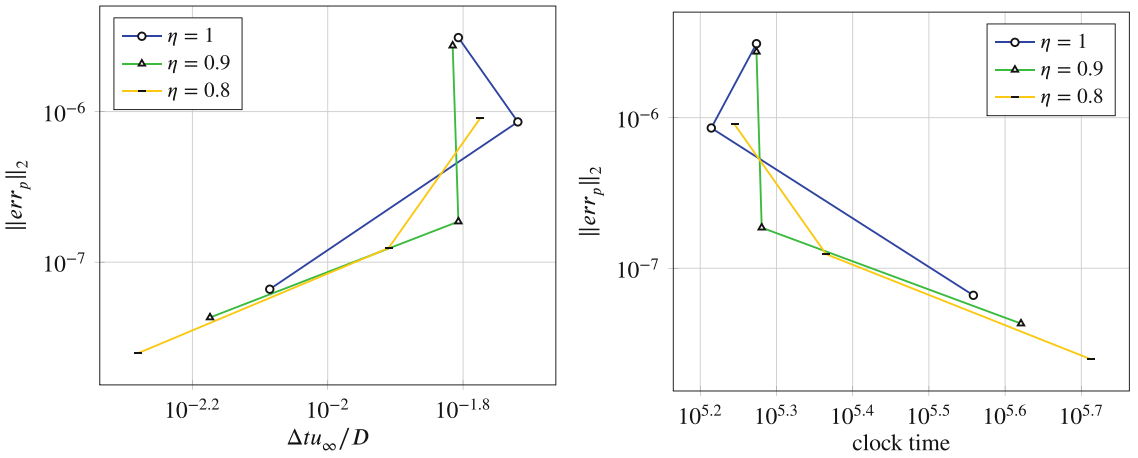

FIGURE 26 Tandem cylinders $Re = 166{,}000$. L^2 norm of the pressure error ($\|err_p\|_2$) as a function of the time-averaged time-step $\Delta tu_\infty / D$ (left) and the clock time (right) with different correction factor η, ROS3PL scheme and H211b controller, $tol_{system} = 10^{-14}$, and discontinuous Galerkin (DG)-$\mathbb{P}^5$ solution approximation

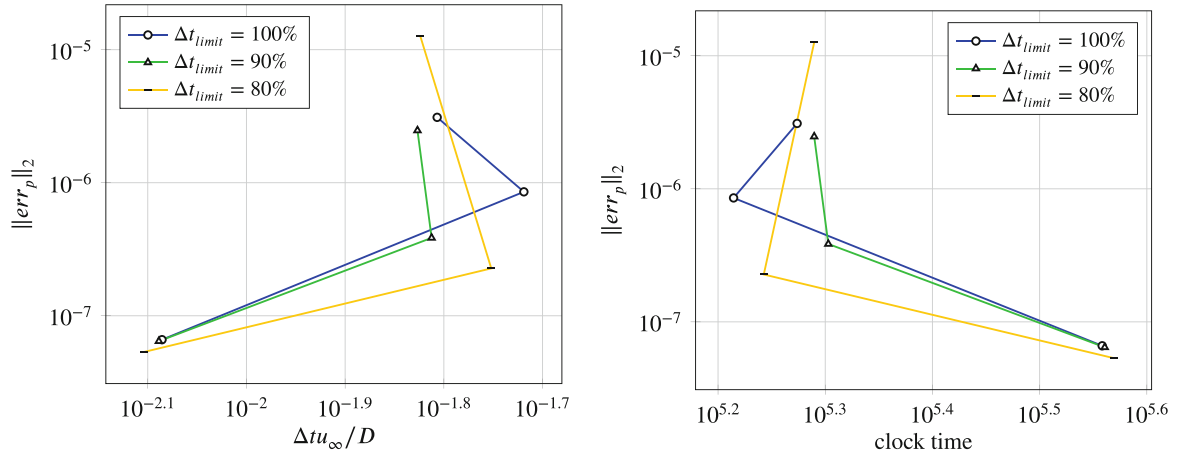

FIGURE 27 Tandem cylinders $Re = 166{,}000$. L^2 norm of the pressure error ($\|err_p\|_2$) as a function of the time-averaged time-step $\Delta tu_\infty / D$ (left) and the clock time (right) with different maximum allowed time-step Δt_{limit}, ROS3PL scheme and H211b controller, $tol_{system} = 10^{-14}$, and discontinuous Galerkin (DG)-$\mathbb{P}^5$ solution approximation

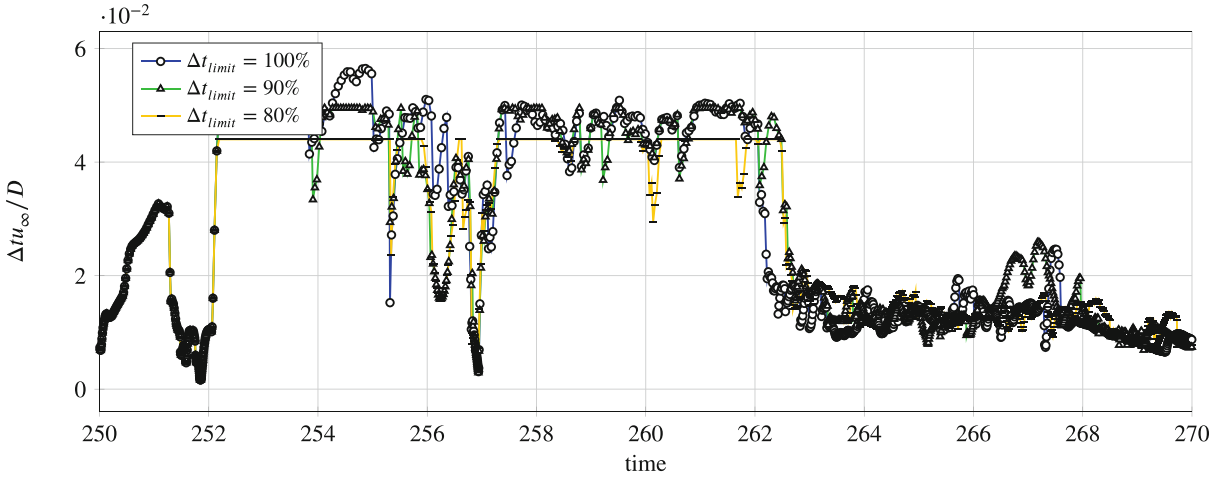

FIGURE 28 Tandem cylinders $Re = 166{,}000$. Time-step $\Delta tu_\infty / D$ evolution with different maximum allowed time-step Δt_{limit}, ROS3PL scheme and H211b controller, $TOL' = 10^{-6}$, $tol_{system} = 10^{-14}$, and discontinuous Galerkin (DG)-$\mathbb{P}^5$ solution approximation

The geometric parameters of the turbine are reported in Table 15. The predicted results are compared with the experimental measurements performed at the Politecnico di Milano low turbulence wind tunnel[16] for different tip speed ratios, $\lambda = \omega\, r/u_\infty$, where r is the radius of the turbine, ω the rotational speed, and u_∞ the wind speed. During the experimental campaign, λ was varied in the range $1.5 < \lambda < 3.5$. The free-stream turbulence intensity was $Tu_\infty = 0.1\%$, while the Reynolds number based on the chord of the airfoils and the angular velocity was $Re = 160{,}000$. The experiments were carried out in a large-scale wind tunnel in both a confined (closed chamber) and unconfined (open chamber) environment. The range of working conditions was obtained by keeping constant the rotational speed $\omega = 500$ rpm of the rotor and by modifying the wind speed u_∞. The maximum rotational speed was limited to avoid structural problems of the turbine rotor, while the minimum wind speed by the measurement accuracy.

Table 16 summarizes the experimental power coefficient c_P for the different tip speed ratios λ in an open chamber.[16] The maximum power coefficient is achieved at 10–11 m/s, corresponding to $\lambda \sim 2.5$. In this condition, the power coefficient is $c_{P\,exp} = 0.311$. For lower velocities (higher λ) a relatively steep reduction of power coefficient occurs, while for higher velocities (lower λ) the reduction is more gradual. Table 16 also reports numerical results by Raciti Castelli et al.[17] of two-dimensional simulations for an open chamber. These numerical results allow to evaluate the influence of the three-dimensional effects of the finite blades length, tip effects, and of the spokes drag on the aerodynamic performance of the turbine. In fact both two- and three-dimensional simulations were performed. The power coefficient of the two-dimensional simulations is roughly 50% larger than the experimental values. As described by Raciti Castelli et al.,[17] this discrepancy is to ascribe to the absence of finite blade length.

The computational mesh has been generated starting from a two-dimensional high-order version of a fully automated in-house hybrid mesh generator based on the advancing-Delaunnay strategy.[25] It is a hybrid mesh with 16,250 triangles and quadrilaterals elements with quadratic edges. The far-field boundary is at 50 chords from the rotation center and the non-dimensional distance of the first mesh line from the wall is equivalent to $y_1^+ \sim 4$. The two-dimensional mesh is then extruded with five elements in the third direction for a c length. The resulting global number of mesh elements is 81,250. At the far-field boundary the freestream condition is imposed, while periodic conditions are considered in the extrusion direction (z axis). The no-slip adiabatic condition is applied to all walls. Simulations are performed with a tip-speed

TABLE 15 VAWT. Geometric characteristics of the turbine, where d is the rotor diameter, h the rotor height, N_b the number of blades, and c the airfoil chord

Profile	NACA 0021
d	1030 mm
h_{rotor}	1456.4 mm
N_b	3
c	85.8 mm

Abbreviation: VAWT, vertical axis wind turbine.

TABLE 16 VAWT. Power coefficient for different tip speed ratios λ obtained by Raciti Castelli et al. from experimental[16] and from numerical[17] investigations

λ	$c_{P\,exp}$	$c_{P\,cfd}$
1.437	0.014	0.171
1.685	0.049	0.250
2.041	0.138	0.424
2.334	0.262	0.532
2.508	0.300	0.552
2.629	0.311	0.566
3.094	0.288	0.548
3.295	0.245	0.518

Abbreviation: VAWT, vertical axis wind turbine.

ratio $\lambda = 1.5$, which represents the most critical flow condition between the operating points of the turbine. This is the minimum value of λ, which corresponds to the maximum freestream velocity. All the computations are performed on a Linux cluster with 10 Intel CascadeLake 8260 CPUs (48 cores per CPU).

Starting from freestream conditions, the first three turbine rotations are simulated with a DG-$\mathbb{P}^1$ solution approximation. Afterwards, the polynomial approximation is switched to $\mathbb{P}^2$, and eighth rotations are performed. Finally, ten rotations are used to average the momentum and power coefficients. In the following the analysis the blades position is identified by the angular coordinate θ of the upper blade chord midpoint with respect to the vertical axis, that is, the y coordinate. In particular, at $\theta = 0°$ the chord midpoint is on the y-axis. The flow problem is periodic on each turbine rotation, and each rotation has a sub-period of one third of the period, since three airfoils are considered. Figures 29 and 30 show the evolution of the instantaneous turbulence intensity and the dissipation rate of the turbulent kinetic energy $\tilde{\omega}$ contours around the turbine during one sub-period. In particular, the azimuthal angles are $\theta = \{0°, 40°, 80°, \text{and} 120°\}$.

Figure 31 shows the evolution of the time-step during one period of the VAWT in comparison with previous two-dimensional incompressible simulation,[4] using the same temporal scheme (ROS3PL) but a different implementation of the adaptive algorithm. Notice the presence of a cyclical behavior with period 120°, which corresponds to the turbine sub-period. Within each sub-period the step size varies of a factor exceeding 3. It is interesting to compare figure 31 with figures 29 and 30. A sudden decrease of Δt is clearly visible around $\theta = 85°$. Near this angle the flow is characterized by

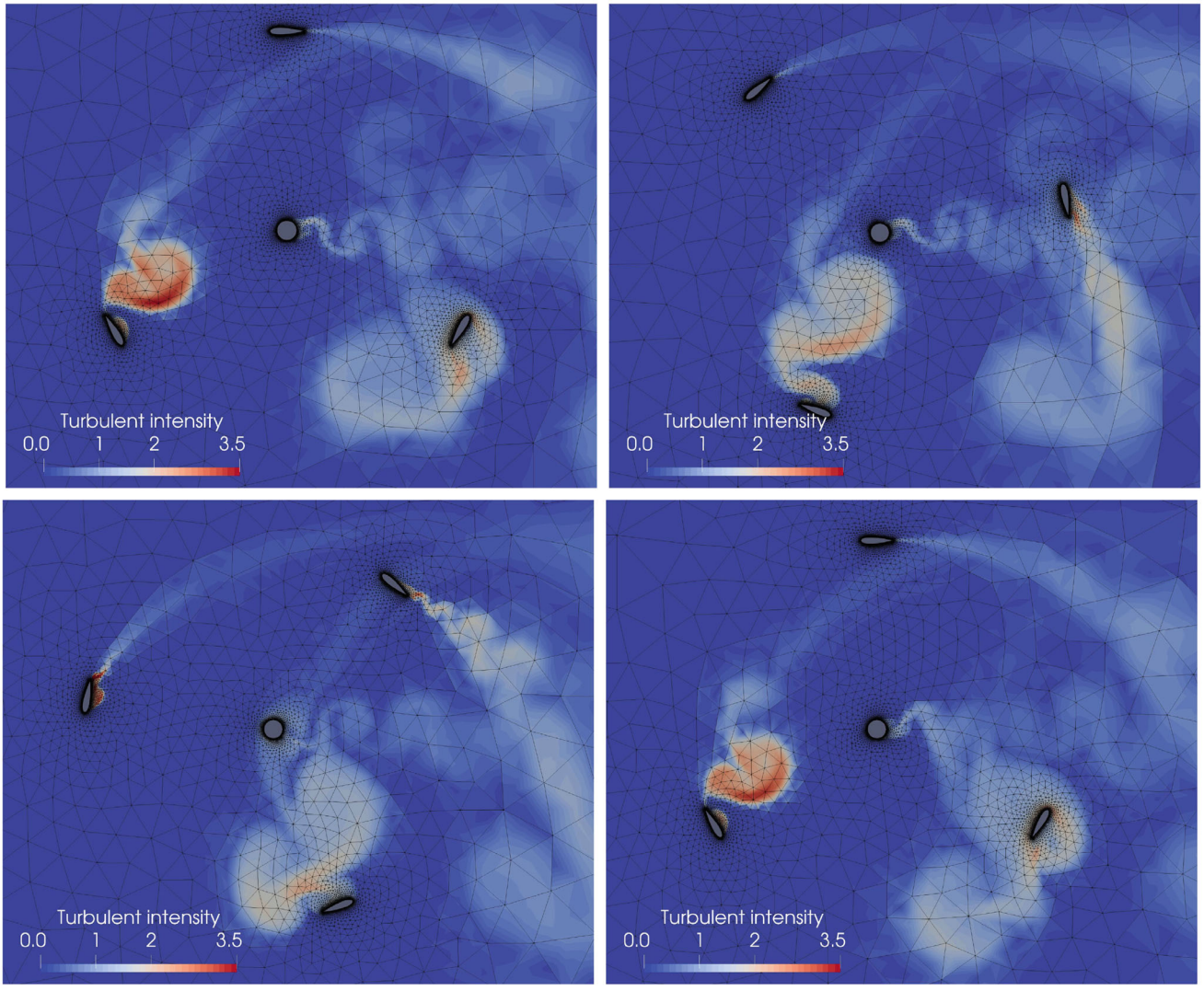

FIGURE 29 Vertical axis wind turbine (VAWT). Evolution of the instantaneous turbulent intensity contours at different azimuthal angles $\theta = 0°$ (top-left), $\theta = 40°$ (top-right), $\theta = 80°$ (bottom-left), and $\theta = 120°$ (bottom-right). Discontinuous Galerkin (DG)-$\mathbb{P}^2$ solution approximation

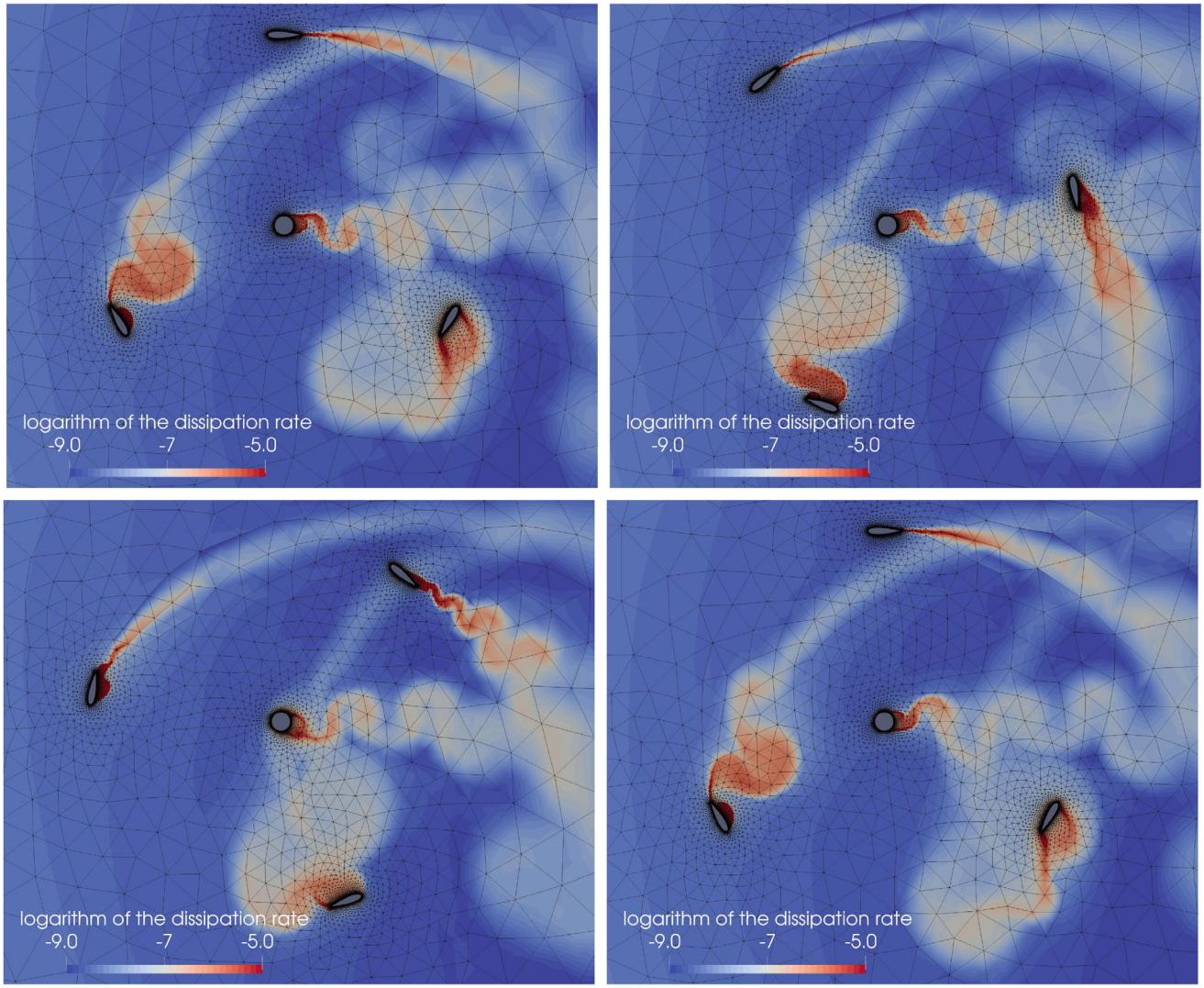

FIGURE 30 Vertical axis wind turbine (VAWT). Evolution of the instantaneous dissipation rate $\tilde{\omega}$ contour at different azimuthal angles $\theta = 0°$ (top-left), $\theta = 40°$ (top-right), $\theta = 80°$ (bottom-left), and $\theta = 120°$ (bottom-right). Discontinuous Galerkin (DG)-$\mathbb{P}^2$ solution approximation.

two main flow features: *i*) the bottom wing profile starts to be perturbed by the detached vortex moving downstream, and *ii*) a growth of the flow instability is evident on the suction side of the upstream wing profile. These phenomena can explain the localized strong reduction of the step width and represent a critical point for the simulation robustness.

The proposed approach allows to successfully compute the unsteady solution using an average time step over one turbine rotation equal to $\Delta t = 0.023 c/u_\infty$, with a maximum time step of $\Delta t_{max} = 0.0475 c/u_\infty$, and a minimum of $\Delta t_{min} = 0.0142 c/u_\infty$. The resulting ratio between the maximum and the minimum time step is ~ 3.34. In the work of Noventa et al.[4] the averaged time step obtained with a different adaptive algorithm is $\Delta t = 0.0038 c/u_\infty$, with a maximum time step $\Delta t_{max} = 0.035 c/u_\infty$, and a minimum $\Delta t_{min} = 0.00012 c/u_\infty$. Although the maximum value is similar, the average time step value is much larger (roughly of a factor 6) with the current adaptation approach. This fact results in a lower global number of steps and thus a lower computational cost ensured by the current approach.

An additional simulation demonstrated also that the maximum allowable fixed time-step is $\Delta t = 0.014 c/u_\infty$. This value is 1.64 times smaller than the average time step obtained with the adaptation strategy. Considering that the rejected steps are $\sim 9.5\%$ of the total steps, it is clear that the adaptation algorithm is an effective way to increase both robustness and efficiency of the simulation.

Table 17 reports the mean value of the power coefficient computed in this work at $\lambda = 1.5$ in comparison with a reference RANS computation[17] and a previous work.[4] Although previous[4] and current simulations share the same temporal

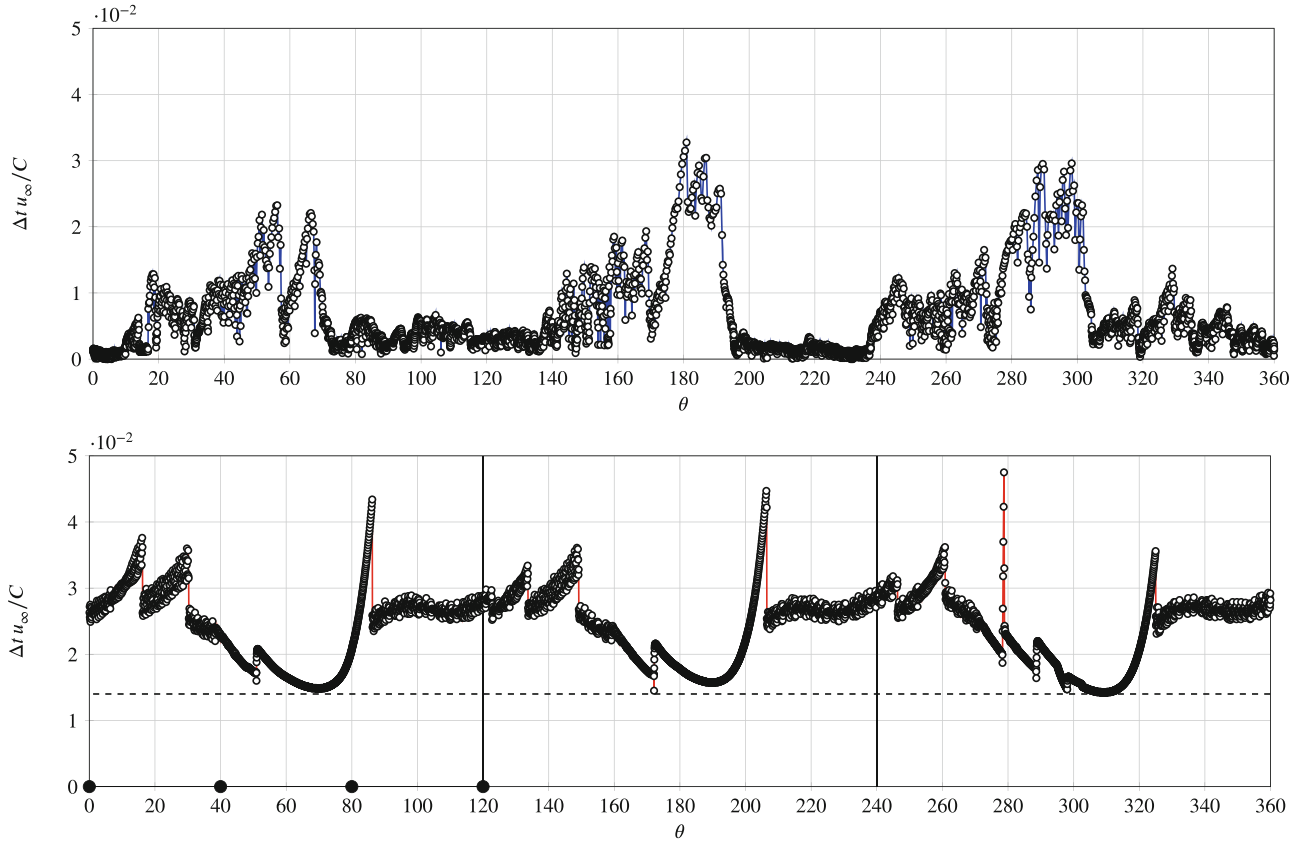

FIGURE 31 Vertical axis wind turbine (VAWT). Non-dimensional time step evolution during one rotation of the turbine with ROS3PL scheme and H21b-smooth controller (bottom) in comparison with Noventa et al.[4] (top). The black vertical lines subdivides the rotation in three part, namely the VAWT sub-periods, while the black dashed horizontal line represent the maximum allowable fixed time-step. The black dots on the horizontal axis represent the angles corresponding to the instantaneous contours depicted in Figures 29 and 30, that is, $\theta = \{0°, 40°, 80°, \text{and} 120°\}$

TABLE 17 VAWT. Comparison of time-averaged power coefficients c_P for the tip speed ratio $\lambda = 1.5$

	c_P		
λ	**Noventa et al.[4]**	**Current work**	**Raciti Castelli et al.[17]**
1.5	0.152	0.173	0.171

Abbreviation: VAWT, vertical axis wind turbine.

scheme, the proposed adaptation algorithm allows to predict results in better agreement with the reference RANS results of Raciti Castelli et al. Notice that, due to the choice of the boundary conditions, the current simulation still neglects the effects of finite blade length, whose analysis is beyond the scope of this work. Numerical investigations comprising wing-tip vortexes are left for future works.

The compressible solver is preferred for the more complex cases since proved to be more efficient. This is strictly related to the efficiency of the solution of the linear system. In fact, due to the nature of DAEs, in the incompressible solver the linear system is worse conditioned resulting in a lower convergence speed in comparison with the compressible solver. Where this outcome becomes more and more prominent as the test case complexity increases.

7 | CONCLUSION

In this work, several adaptive time step strategies coupled with high-order linearly implicit time integration schemes are investigated and critically compared in a discontinuous Galerkin discretization of compressible and

TABLE 18 Comparison of the near-stability zone (highest solution error) in terms of pressure error $\|err_p\|_2$, clock time and rejected time-steps variation (with respect to a fixed step size) for the different controllers, the ROS3PL scheme, $tol_{System} = 10^{-16}$, and DG-$\mathbb{P}^5$ solution approximation

	Controller	$\Delta_{\|err_p\|_2}$ [%]	$\Delta_{\text{clock time}}$ [%]	Rejected time-step [%]
Cylinder $Re = 3900$ (comp.)	Standard	849.58	−38.92	8.76
	PI 4.2	1547.06	−23.24	9.45
	H211b	2984.03	8.65	8.80
	H211b-smooth	925.21	7.57	10.53
	H312b	1622.69	−25.95	8.99
Cylinder $Re = 3900$ (inc.)	Standard	4876.08	−69.43	7.40
	PI 4.2	7220.57	−79.81	9.02
	H211b	5689.47	−75.28	9.20
	H211b-smooth	6167.94	−75.28	8.36
	H312b	6885.65	−76.98	9.68
Cylinder $Re = 140,000$	Standard	768.62	−9.56	7.96
	PI 4.2	1647.54	−5.08	10.55
	H211b	368.46	−11.98	7.30
	H211b-smooth	2437.46	26.58	9.03
	H312b	1767.17	23.46	10.59
Tandem cylinders $Re = 166,000$	Standard	4411.45	30.77	8.30
	PI 4.2	6991.60	6.67	9.55
	H211b	2266.41	−3.59	9.68
	H211b-smooth	16388.55	147.69	9.44
	H312b	7426.72	23.08	8.35

incompressible unsteady RANS equations. Several test cases with increasing stiffness and difficulty are considered: the turbulent flow around a circular cylinder at two different Reynolds numbers $Re = \{3900, 140,000\}$, the flow around a tandem cylinders at $Re = 166,000$, and, finally, the turbulent flow through a VAWT at $Re = 160,000$.[16,17] The time integration schemes used are: the linearly implicit one-step Rosenbrock-type Runge–Kutta of third order/three stages ROS3PL,[9] fourth order/six stages RODASP,[10] and fifth order/eight stages ROD5_1,[11] and the linearly implicit Rosenbrock-type two-step peer schemes.[6,12] The controllers applied within the adaptation strategy are: the standard,[13] the PI 4.2,[14] and the H211b and H312b.[15] In addition, a smooth limiter function, a correction factor and a maximum step size limit are introduced.

All the analysed combinations between adaptive controllers and temporal schemes showed a performance comparable with fixed time step simulations for small step sizes, that is, when small local truncation errors are considered. This outcome suggests that the use of the adaptive strategy is of little use when small time step width is preferred for the simulation. Conversely, the adaptive strategy revealed its usefulness with higher time step values. In particular, the time adaptation increased the simulation robustness since allowed to achieve errors, and thus step sizes, larger than the limit given by the near-stability zone with fixed time steps. Moreover, although higher adaptive tolerances led to a higher fraction of rejected steps and, thus, to a possible increase of the computational cost, see Table 18, an optimal test case dependent threshold for the tolerance can be found, see Table 19. This optimal choice allows to exploit both robustness and efficiency enhancements for all the unsteady RANS simulations considered.

The unsteady turbulent flow through a vertical axis turbine is simulated with the ROS3PL scheme and the H211b controller. Numerical results showed a good agreement with reverence unsteady RANS simulations. For this test case the adaptation algorithm proposed in this work proved to be effective in increasing the robustness and the efficiency of the time integration with respect to a constant step size and to a previous adaptive strategy applied to the same test case. This case represents an industrial case which involves the computation of a strongly unsteady flow characterized by a wide

TABLE 19 Comparison of the optimal point (lowest clock-time) in terms of pressure error $\|err_p\|_2$, clock time and rejected time-steps variation (with respect to a fixed step size) for the different controllers, the ROS3PL scheme, $tol_{System} = 10^{-16}$ and DG-$\mathbb{P}^5$ solution approximation

	controller	$\Delta_{\|err_p\|_2}$ [%]	$\Delta_{\text{clock time}}$ [%]	rejected time-step [%]
Cylinder $Re = 3\,900$ (comp.)	standard	849.58	−38.92	8.76
	PI 4.2	908.40	−43.24	3.65
	H211b	942.02	−37.84	2.17
	H211b-smooth	925.21	7.57	10.53
	H312b	900.00	−52.27	3.32
Cylinder $Re = 3\,900$ (inc.)	standard	4876.08	−69.43	7.40
	PI 4.2	7220.57	−79.81	9.02
	H211b	5689.47	−75.28	9.20
	H211b-smooth	6167.94	−75.28	8.36
	H312b	6885.65	−76.98	9.68
Cylinder $Re = 140\,000$	standard	768.62	−9.56	7.96
	PI 4.2	701.67	−20.89	4.59
	H211b	368.46	−11.98	7.30
	H211b-smooth	773.84	−23.33	2.42
	H312b	730.51	−16.15	5.08
Tandem cylinders Re = 166 000	standard	445.04	−11.79	5.15
	PI 4.2	483.97	−15.38	3.91
	H211b	551.91	−15.90	4.18
	H211b-smooth	2266.41	−3.59	3.11
	H312b	483.97	−15.38	3.19

range of spatial and temporal scales over (very) long time periods, and on cases like this an adaptive time-step is extremely important to achieve an high computational efficiency with a user-defined level of accuracy.

The work is in progress to extend the feasibility of the adaptive time integration for hybrid RANS-LES methods,[49-51] which are spreading in many research areas for the reduced computational cost with respect to the LES approach. In fact in hybrid approaches a robust, accurate, and efficient time integration is required to merge the LES and RANS formulations, without a reduction of the maximum allowable fixed time-step.

DATA AVAILABILITY STATEMENT

The data that support the findings of this study are available from the corresponding author upon reasonable request.

ENDNOTE

*-n 250,000 -s 10 define the reference TauBench workload for the hardware benchmark.

ACKNOWLEDGMENT

Open Access Funding provided by Universita degli Studi di Brescia within the CRUI-CARE Agreement.

ORCID

Gianmaria Noventa https://orcid.org/0000-0002-7668-4539

REFERENCES

1. Bassi F, Botti L, Colombo A, et al. Time Integration in the discontinuous Galerkin code MIGALE–Unsteady problems. In: Kroll N, Hirsch C, Bassi F, Johnston C, Hillewaert K, eds. *IDIHOM: Industrialization of High-Order Methods–A Top-Down Approach 128 of Notes on Numerical Fluid Mechanics and Multidisciplinary Design*. Springer International Publishing; 2015:205-230.

2. Antoniadis A, Tsoutsanis P, Drikakis D. Assessment of high-order finite volume methods on unstructured meshes for RANS solutions of aeronautical configurations. *Comput Fluids* 2017; 146: 86-104. 10.1016/j.compfluid.2017.01.002.
3. Bassi F, Botti L, Colombo A, Ghidoni A, Massa F. Linearly implicit Rosenbrock-type Runge–Kutta schemes applied to the discontinuous Galerkin solution of compressible and incompressible unsteady flows. *Comput Fluids*. 2015;118:305-320. doi:10.1016/j.compfluid.2015.06.007.
4. Noventa G, Massa F, Bassi F, Colombo A, Franchina N, Ghidoni A. A high-order discontinuous Galerkin solver for unsteady incompressible turbulent flows. *Comput Fluids*. 2016;139:248-260. 13th USNCCM International Symposium of High-Order Methods for Computational Fluid Dynamics–A special issue dedicated to the 60th birthday of Professor David Kopriva. 10.1016/j.compfluid.2016.03.007.
5. Bassi F, Colombo A, De Bartolo C, Franchina N, Ghidoni A, Nigro A. Investigation of high-order temporal schemes for the discontinuous Galerkin solution of the Navier–Stokes equations. 11th World Congress on Computational Mechanics, WCCM 2014, 5th European Conference on Computational Mechanics, ECCM 2014 and 6th European Conference on Computational Fluid Dynamics. *ECFD*. 2014;2014:5651-5662.
6. Massa F, Noventa G, Lorini M, Bassi F, Ghidoni A. High-order linearly implicit two-step peer schemes for the discontinuous Galerkin solution of the incompressible Navier–Stokes equations. *Comput Fluids*. 2018;162:55-71. doi:10.1016/j.compfluid.2017.12.003.
7. Noventa G, Massa F, Rebay S, Bassi F, Ghidoni A. Robustness and efficiency of an implicit time-adaptive discontinuous Galerkin solver for unsteady flows. *Comput Fluids* 2020; 204: 104529. 10.1016/j.compfluid.2020.104529.
8. Noventa G, Massa F, Rebay S, Colombo A, Bassi F, Ghidoni A. Investigation of adaptive time-step strategies for high-order accurate incompressible simulations. Paper presented at: 6th European Conference on Computational Mechanics (ECCM 6), 7th European Conference on Computational Fluid Dynamics (ECFD 7), 2018, Glasgow (UK).
9. Lang J, Teleaga D. Towards a fully space-time adaptive FEM for magnetoquasistatics. *IEEE Trans magn.* 2008;44:1238-1241. doi:10.1109/TMAG.2007.914837.
10. Steinebach G. *Order-reduction of ROW-methods for DAEs and method of lines applications*. Techn. Hochsch., Fachbereich Mathematik; 1995:1995.
11. Marzo GD. RODAS5(4)-Méthodes de Rosenbrock d'ordre 5(4) adaptées aux problemes différentiels-algébriques. MSc Mathematics Thesis, Faculty of Science, University of Geneva, Switzerland; 1993.
12. Massa F, Noventa G, Bassi F, Colombo A, Ghidoni A, Lorini M. High-order linearly implicit two-step peer methods for the discontinuous Galerkin solution of the incompressible rans equations. 2016;2:2664-2683. ECCOMAS Congress 2016-Proceedings of the 7th European Congress on Computational Methods in Applied Sciences and Engineering. 10.7712/100016.1988.8180.
13. Hairer E, Wanner G. *Solving Ordinary Differential Equations II*. Springer Series in Computational Mathematics; 1996.
14. Gustafsson K, Lundh M, Söderlind G. A PI Stepsize Control for the Numerical Solution of Ordinary Differential Equations. *BIT Comput Sci Numer Math*. 1988;28(2):270-287. doi:10.1007/BF01934091.
15. Söderlind G. Digital Filters in Adaptive Time-Stepping. *ACM Trans. Math. Softw.* 2003;29:1-26. doi:10.1145/641876.641877.
16. Dossena V, Persico G, Paradiso B, et al. An Experimental Study of the Aerodynamics and Performance of a Vertical Axis Wind Turbine in a Confined and Unconfined Environment. *J Energy Resour Technol*. 2015;137(5):051207.
17. Raciti Castelli M, Englaro A, Benini E. The Darrieus wind turbine: Proposal for a new performance prediction model based on CFD. *Energy*. 2011;36(8):4919-4934. PRES 2010. doi:10.1016/j.energy.2011.05.036.
18. Bassi F, Ghidoni A, Perbellini A, et al. A high-order discontinuous Galerkin solver for the incompressible RANS and k − ω turbulence model equations. *Comput Fluids*. 2014;98:54-68.
19. Ricci F, Silva P, Tsoutsanis P, Antoniadis A. Hovering rotor solutions by high-order methods on unstructured grids. *Aerosp Sci Technol*. 2020;97:105648. doi:10.1016/j.ast.2019.105648.
20. Silva P, Tsoutsanis P, Antoniadis A. Simple multiple reference frame for high-order solution of hovering rotors with and without ground effect. *Aerosp Sci Technol*. 2021;111:106518. doi:10.1016/j.ast.2021.106518.
21. Bassi F, Botti L, Colombo A, Di Pietro D, Tesini P. On the flexibility of agglomeration based physical space discontinuous Galerkin discretizations. *J Comput Phys*. 2012;231(1):45-65. doi:10.1016/j.jcp.2011.08.018.
22. Gerisch A, Lang J, Podhaisky H, Weiner R. High-order linearly implicit two-step peer-finite element methods for time-dependent PDEs. *Appl Numer Math* 2009; 59(34): 624-638. Selected Papers from NUMDIFF-11.
23. Podhaisky H, Weiner R, Schmitt B. Rosenbrock-type Peer two-step methods. *Appl Numer Math*. 2005;53:409-420. Dedicated to Profesor Karl Strehmel, on the occasion of his 70th birthday.
24. Soderlind G, Wang L. Adaptive time-stepping and computational stability. *J Comput Appl Math*. 2006;185(2):225-243. Special Issue: International Workshop on the Technological Aspects of Mathematics.
25. Ghidoni A, Pelizzari E, Rebay S, Selmin V. 3D anisotropic unstructured grid generation. *Int. J. Numer. Meth. Fl.* 2006;51(9-10):1097-1115. doi:10.1002/fld.1151.
26. Simmendinger C, Versick D. Integrated Performance Analysis of Computer Systems (IPACS). Benchmarks for Distributed Computer Systems. *Praxis der Informationsverarbeitung und Kommunikation*. 2005;28(3):150-159.
27. Rajani BN, Kandasamy A, Majumdar S. LES of Flow past Circular Cylinder at Re = 3900. *J Appl Fluid Mech*. 2016;9:1421-1435. doi:10.18869/acadpub.jafm.68.228.24178.
28. Norberg C. Flow around a circular cylinder: aspects of fluctuting lift. *J Fluids Struct*. 2001;15(3):459-469.
29. Son JS, Hanratty TJ. Velocity gradients at the wall for flow around a cylinder at Reynolds numbers from 5 × 103 to 105. *J Fluid Mech*. 1969;35(2):353-368. doi:10.1017/S0022112069001157.

30. Ong L, Wallace J. The velocity field of the turbulent very near wake of a circular cylinder. *Exp Fluids*. 1996;20(6):441-453. doi:10.1007/BF00189383.
31. Parnaudeau P, Carlier J, Heitz D, Lamballais E. Experimental and numerical studies of the flow over a circular cylinder at Reynolds number 3900. *Phys Fluids*. 2008;20(8):085101. doi:10.1063/1.2957018.
32. Kravchenko AG, Moin P. Numerical studies of flow over a circular cylinder at ReD=3900. *Phys Fluids*. 2000;12(2):403-417. doi:10.1063/1.870318.
33. Wissink J, Rodi W. Numerical study of the near wake of a circular cylinder. *Int J Heat Fluid Flow*. 2008;29:1060-1070. doi:10.1016/j.ijheatfluidflow.2008.04.001.
34. Lysenko DA, Ertesvåg IS, Rian KE. Large-Eddy simulation of the flow over a circular cylinder at reynolds number 3900 using the OpenFOAM toolbox. *Flow, Turbulence and Combustion*. 2012;89(4):491-518. doi:10.1007/s10494-012-9405-0.
35. Ma X, Karamanos GS, Karniadakis GE. Dynamics and low-dimensionality of a turbulent near wake. *J Fluid Mech*. 2000;410:29-65. doi:10.1017/S0022112099007934.
36. Breuer M. Large eddy simulation of the subcritical flow past a circular cylinder: numerical and modeling aspects. *Int J Numer Methods Fluids*. 1998;28(9):1281-1302.
37. Shur M. Strelets M., Travin A. Navier-Stokes simulation of shedding turbulent flow past a circular cylinder and a cylinder with backward splitter plate. 1996.
38. Roshko A. Experiments on the flow past a circular cylinder at very high Reynolds number. *J Fluid Mech*. 1961;10(3):345-356.
39. Achenbach E. Influence of surface roughness on the cross-flow around a circular cylinder. *J Fluid Mech*. 1971;46(2):321-335.
40. Fage A, Falkner V. *Further Experiments on the Flow around a Circular Cylinder*. His Majesty's Stationery Office; 1931.
41. Giedt W. Effect of turbulence level of incident air stream on local heat transfer and skin friction on a cylinder. *J Aeron Sci*. 1951;18(11):725-730.
42. Fröhlich J, Rodi W, Kessler P, Parpais S, Bertoglio JP, Laurence D. *Large Eddy Simulation of Flow around Circular Cylinders on Structured and Unstructured Grids: 319-338; Berlin*. Springer Berlin Heidelberg; 1998.
43. Fröhlich J, Rodi W, Bertoglio JP, Bieder U, Touil H. *Large Eddy Simulation of Flow around Circular Cylinders on Structured and Unstructured Grids*, II. Notes on Numerical Fluid Mechanics. Springer; 2001.
44. Shur M, Spalart P, Strelets M, Travin A. Detached-eddy simulation of an airfoil at high angle of attack. In: Rodi W, Laurence D, eds. *Engineering Turbulence Modelling and Experiments 4*. Elsevier Science Ltd.; 1999:669-678.
45. Islam A, Thornber B. A High-Order Hybrid Turbulence Model with Implicit Large-Eddy Simulation. *Comput Fluids*. 2018;167:292-312. doi:10.1016/j.compfluid.2018.03.031.
46. Cantwell B, Coles D. An experimental study of entrainment and transport in the turbulent near wake of a circular cylinder. *J Fluid Mech*. 1983;136:321-374.
47. Moussaed C, Vittoria Salvetti M, Wornom S, Koobus B, Dervieux A. Simulation of the flow past a circular cylinder in the supercritical regime by blending RANS and variational-multiscale LES models. *J Fluids Struc*. 2014;47:114-123. Special Issue on Unsteady Separation in Fluid-Structure Interaction-l. 10.1016/j.jfluidstructs.2013.11.006.
48. Khorrami M, Choudhari M, Lockard D, Jenkins L, McGinley C. Unsteady Flowfield Around Tandem Cylinders as Prototype Component Interaction in Airframe Noise. *Aiaa J*. 2007;45:1930-1941. doi:10.2514/1.23690.
49. Bassi F, Botti A, Colombo A, Ghidoni A, Massa F, Noventa G. On the development of an implicit high-order discontinuous Galerkin solver for a hybrid RANS-LES model. In: *Direct and Large-Eddy Simulation XI*. Vol 25. Springer; 2019:75-82.
50. Bassi F, Colombo A, Ghidoni A, Noventa G. Implementation of a wall-distance-free composite RANS-ILES model in a high-order discontinuous Galerkin solver. *Direct and Large Eddy Simulation XII*. Vol 27. Springer; 2020:357-363.
51. Bassi F, Colombo A, Massa FC, Noventa G, Ghidoni A. Hybrid RANS-LES simulations with the discontinuous Galerkin method. Paper presented at: 6th European Conference on Computational Mechanics (ECCM 6), 7th European Conference on Computational Fluid Dynamics (ECFD 7), 2018, Glasgow(UK).

How to cite this article: Ghidoni A, Massa FC, Noventa G, Rebay S. Assessment of an adaptive time integration strategy for a high-order discretization of the unsteady RANS equations. *Int J Numer Meth Fluids*. 2022;1-41. doi: 10.1002/fld.5131